Supporting Information

Cosolvent Occupied Solvation Tuned Anti-Oxidation Therapy Toward Highly Safe 4.7V-Class NCM811 Battery

Yuqing Chen[1], Yun Zhao[2], Aiping Wang[3], Daozhen Zhang[4], Baohua Li[2], Xiangming He[3], Xiulin Fan[5], Jilei Liu[1*]

[1]*College of Materials Science and Engineering, Hunan Joint International Laboratory of Advanced Materials and Technology of Clean Energy, Hunan Province Key Laboratory for Advanced Carbon Materials and Applied Technology, Hunan University, Changsha 410082, People's Republic of China*

[2]*Shenzhen Key Laboratory on Power Battery Safety and Shenzhen Geim Graphene Center, Tsinghua Shenzhen International Graduate School (SIGS), Shenzhen 518055, China*

[3]*Institute of Nuclear and New Energy Technology, Tsinghua University, Beijing 100084, China*

[4]*School of Chemical Engineering, Anhui University of Science and Technology, Huainan, 232001, China.*

[5]*State Key Laboratory of Silicon Materials, School of Materials Science and Engineering, Zhejiang University, Hangzhou 310027, China*

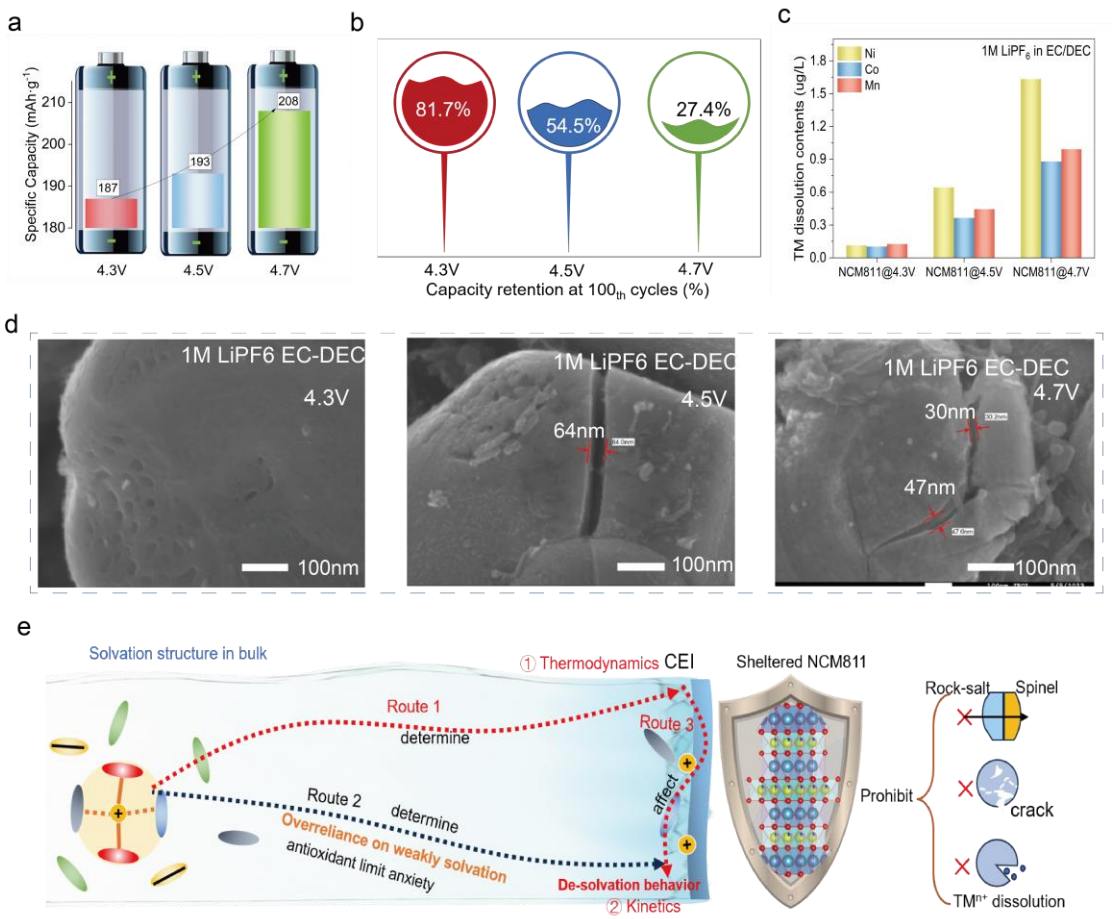

Fig. S1. a, Cut-off voltage dependent specific capacity for NCM811 cells. b, Capacity retention of NCM811 cells at 100th cycle with different cut-off voltages. c, TM dissolution content of the graphite anode after 100 cycles in NCM811/Gr cells. d, The corresponding SEM images of NCM811 cathode after 100 cycles. e, The triangle relationship between solvation structure, CEI formation and de-solvation process, and its role for sheltering NCM811.

Theoretically, ions transfer either in electrolyte or interface is highly related to the solvation structure, during which CEI formation (route 1) and desolvation (route 2) are the two key processes to determine the high voltage performance. The former controls whether the CEI can withstand high voltage or not, which is on the thermodynamics level, while the later determines the kinetics process such as charge transfer. Since the CEIs counts for the desolvation, solvation structure design should focus on the CEI regulation instead of weak solvation. And an anion-enrichment interface is reported to aids ion de-solvation[1, 2]. The relationship between solvation structure, CEIs and de-solvation can be described as a triangle, and we focus more on the two sides of the triangle with red line instead of the black line (**Fig. S1e**). Therefore, the cycled NCM811

cathode under deep de-lithiation is expected to be well sheltered to avoid the unwanted changes such as irreversible phase transition, cracks, and TM ions dissolution, which are fatal to run under high voltage (**Fig. S2g**).

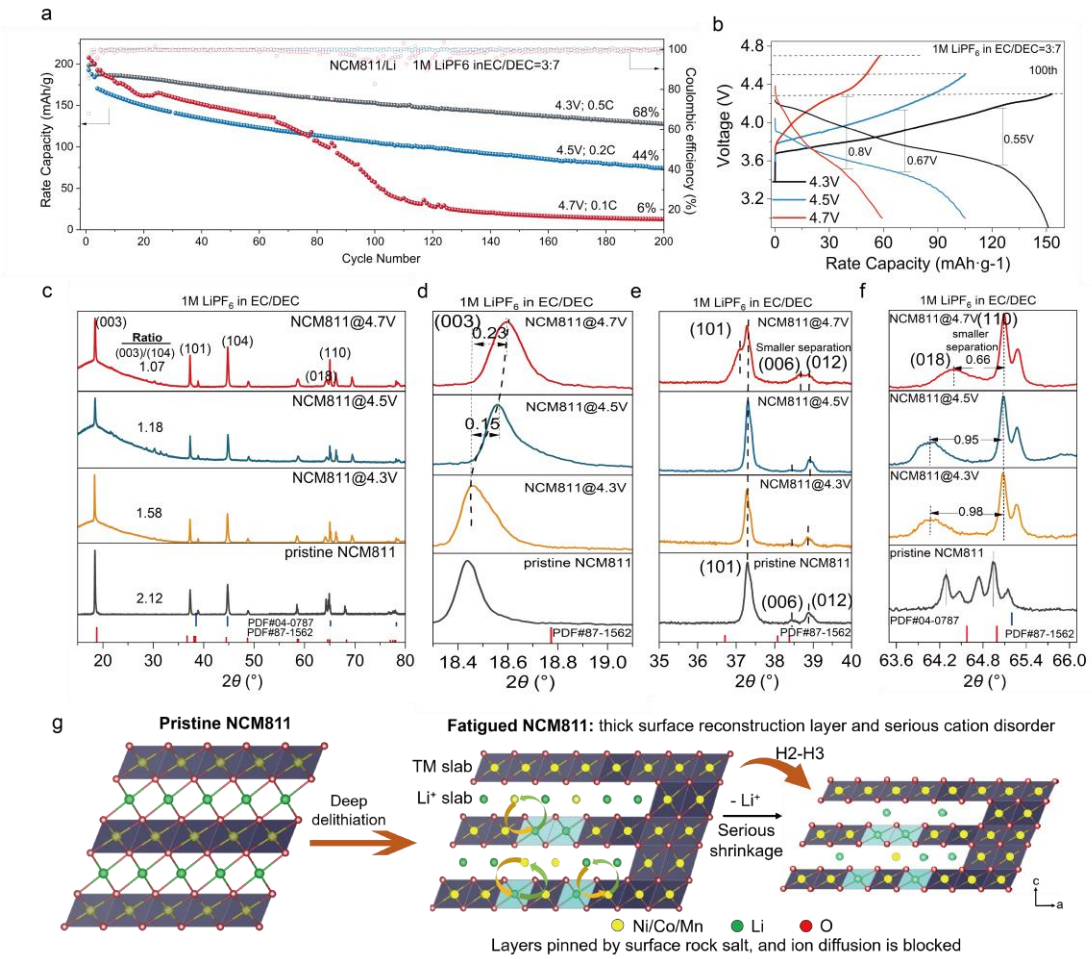

Fig. S2: a, Long cycle performance of NCM811 with EC-DEC electrolytes. b, the corresponding charge and discharge profiles. c, the XRD pattern of NCM811 cathode after 100 cycles under deep de-lithiation with the cutoff voltage of 4.3V, 4.5V and 4.7V. d-f, the corresponding local XRD spectrum for (003) plane (d), and (101) plane (e), and (110) plane (f). g, Schematic diagram of NCM811 materials after long cycle under deep de-lithiation.

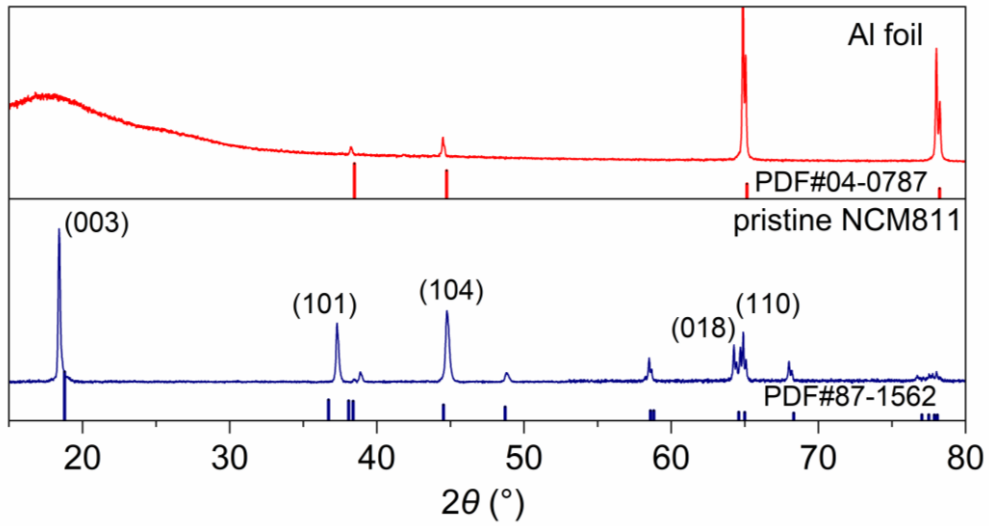

Fig. S3: a, The XRD pattern of Al foil and pristine NCM811 cathode.

The (003) peaks greatly shift right which corresponds to a phase transition from H2 to H3 phase with a reduced interlayer spacing as the cutoff voltage increased from 4.3V to 4.5V and 4.7V in the EC-DEC electrolyte (**Fig. S2d**). Moreover, the separation of (006)/(012) and (018)/(110) peaks is more close for the cycled NCM811 with EC-DEC electrolyte with the voltage increased, indicating the structure transformation from layered to rock salt phase under deep de-lithiation operation (**Fig. S2e-f**). This result confirms that the cycled NCM811 cathode with commercial carbonated electrolyte presents a much irreversible structural evolution, which intensifies during cycle. More importantly, the lower intensity ratio of $I_{(003)}/I_{(104)}$ as the cutoff voltage increased suggests a serious cation-ion mixing and incomplete layer structure under deep de-lithiation operation (**Fig S2g**).

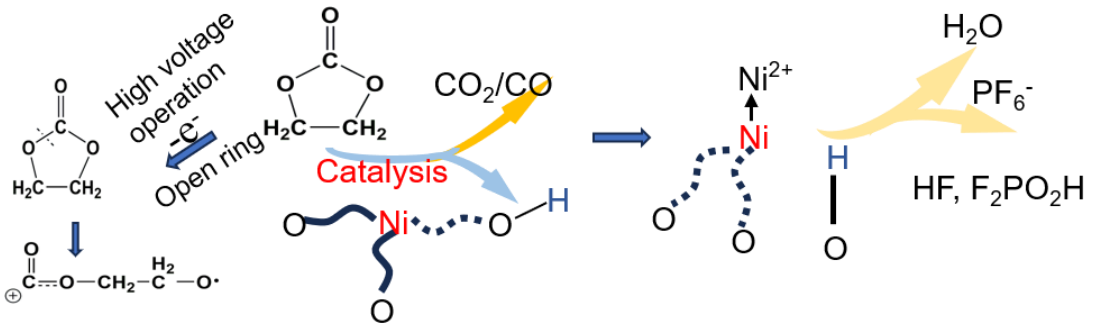

Fig. S4: Scheme of EC oxidation decomposition and $Ni_{lattice}$ catalysis and the release of TM ions on the cathode side.

The main culprit for the structure issue is highly related to ethylene carbonate (EC) which is one of the least oxidation-resistant carbonate solvents, thus exerting adverse

effect on the electrochemical properties for high voltage cathodes by forming a less robust CEI layer, because the electrolyte decomposition species including inorganic and oxygenated organic compounds on the cathode surface are related to EC or solvated EC decomposition. On one hand, under high voltage operation, EC's ring opening reaction catalyzed by the de-lithiated cathode surface and PF_5 Lewis acid leads to the formation of CEI layers composed of an organic and organo-fluorine film. On the other hand, Ni catalyzes solvent decomposition, forming proton-containing side products, then the side products and dissolved nickel ions both cross to the anode side, resulting in the destruction of the SEI and impedance growth, and forming H_2 (**Fig S3**).

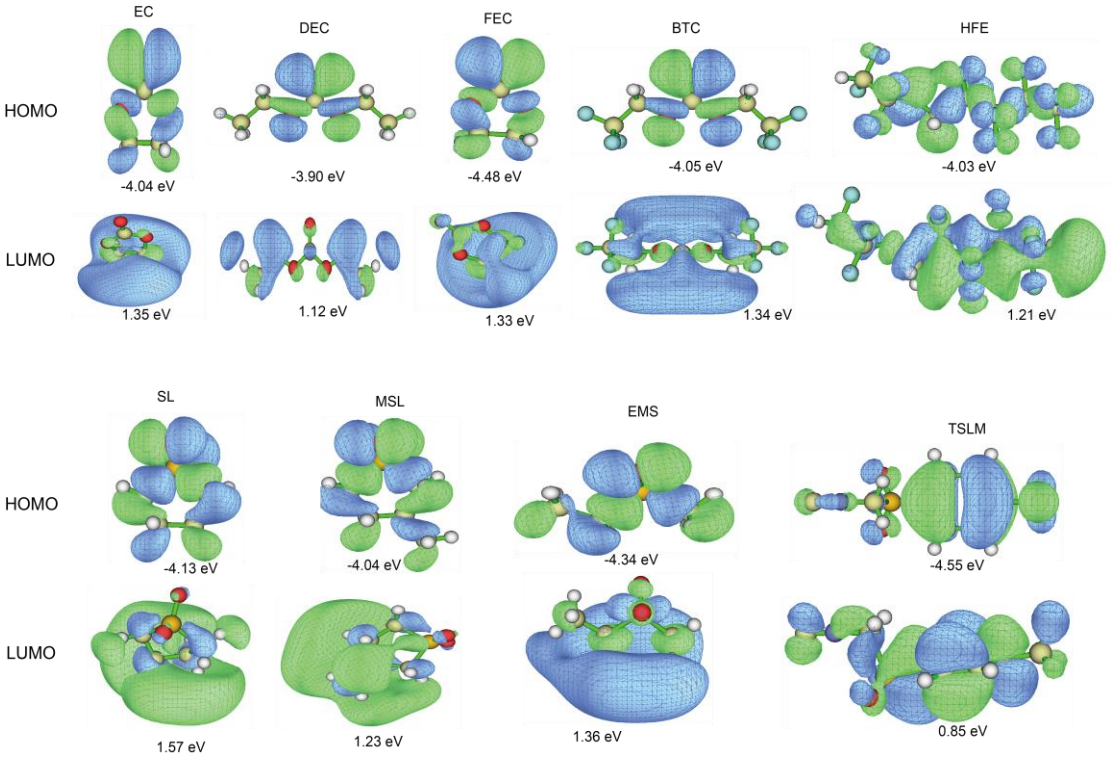

Fig. S5: HOMO and LUMO energies of carbonated solvents and the possible sulfone solvents.

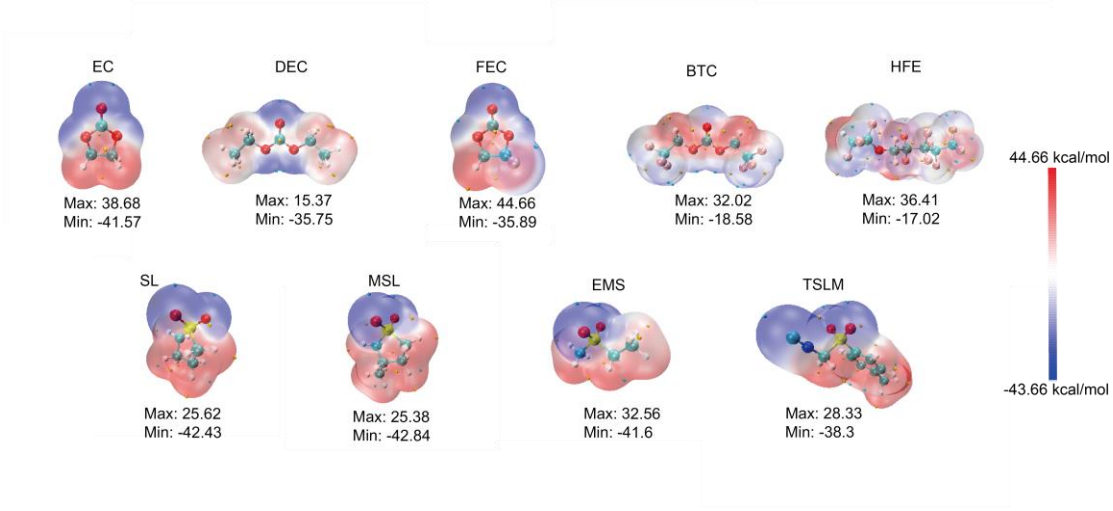

Fig. S6: Electrostatic potential distribution of the common solvents and the screened sulfone solvents.

Among the selected sulfone solvents, compared with fluorinated solvent whose $|ESP_{min}| < ESP_{max}$, sulfolane (SL) and 3-methylsulfolane (MSL) with more negative ESP_{min}, suggesting their stronger coordination ability with Li^+, and SL and MSL are competing to occupy the solvation site of fluorinated main solvents such as fluorinated ethylene carbonate (FEC) and bis(2,2,2-trifluorethyl) carbonate (BTC). In EC-DEC electrolyte, for EC, $|ESP_{min}| \approx |ESP_{max}|$, EC is strongly coordinated with Li^+, while for DEC, the $|ESP_{min}| > |ESP_{max}|$, DEC is relative weak solvation solvent. Similarly, in FBH electrolyte, FEC is strong solvation solvent compared with BTC, and for HFE, the $|ESP_{min}| < |ESP_{max}|$, suggesting the antisolvent characteristic of HFE.

Furthermore, the interaction of solvent with additive anion ($DFOB^-$) is evaluated to judge whether the $DFOB^-$ can be given the chance to be oxidated in replacement of co-solvent (**Fig. 1d, Fig. S7**). Among the selected sulfone solvents, SL takes the great advantages of higher interaction with $DFOB^-$, which indicates that SL can make way to $DFOB^-$ to be fully oxidated. Therefore, the interaction relationship among Li^+- solvent -anion need to be defined in the co-solvent occupancy strategy to design rational solvation structure, which can be described as follows: i) Li^+ - co-solvent > Li^+- main solvent; ii) $DFOB^-$ - co-solvent > $DFOB^-$ - main solvent, iii) $DFOB^-$ - co-solvent > $DFOB^-$ - Li^+ (**Fig. 1e**).

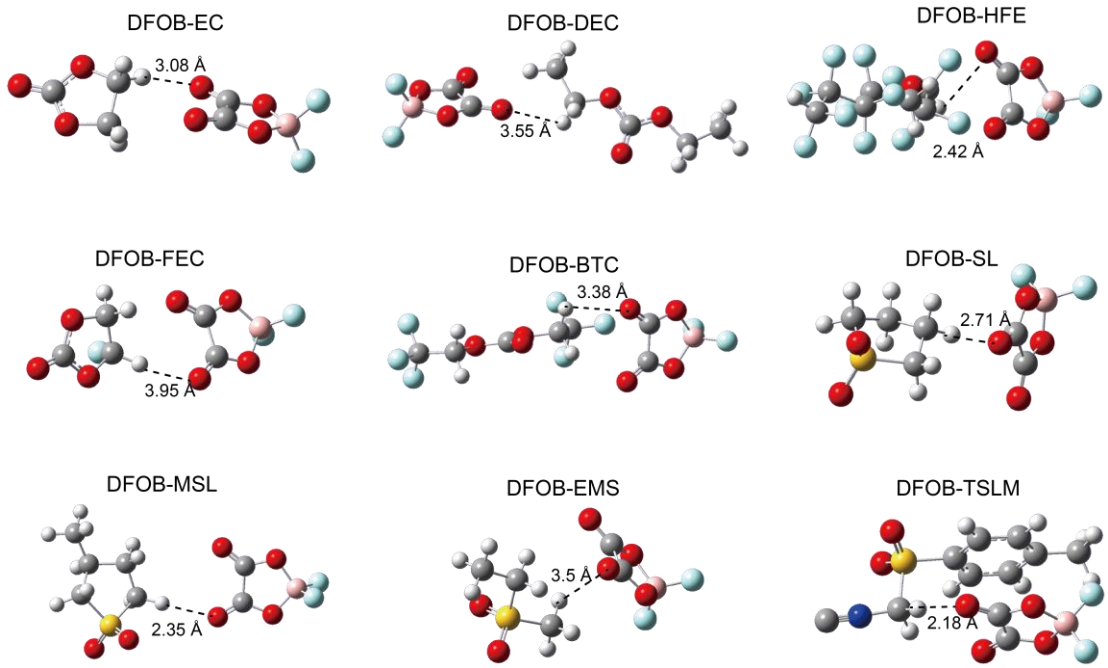

Fig. S7: Interaction energy of $DFOB^-$ with carbonated solvents and the possible sulfone solvents.

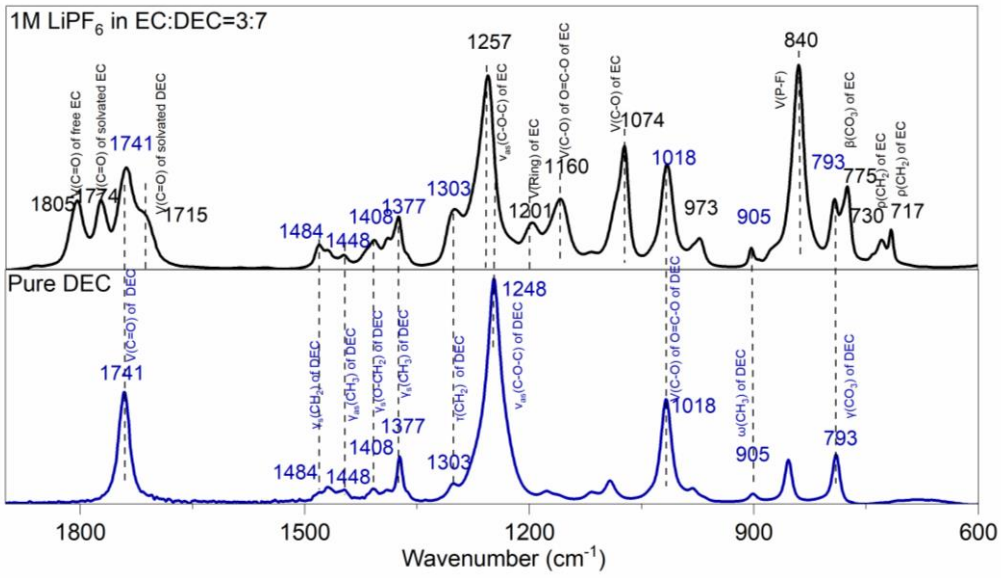

Fig. S8: Full FTIR spectra of EC-DEC electrolyte and the corresponding pure DEC solvent, to confirm the assignment of peak positions in the mixed solution.

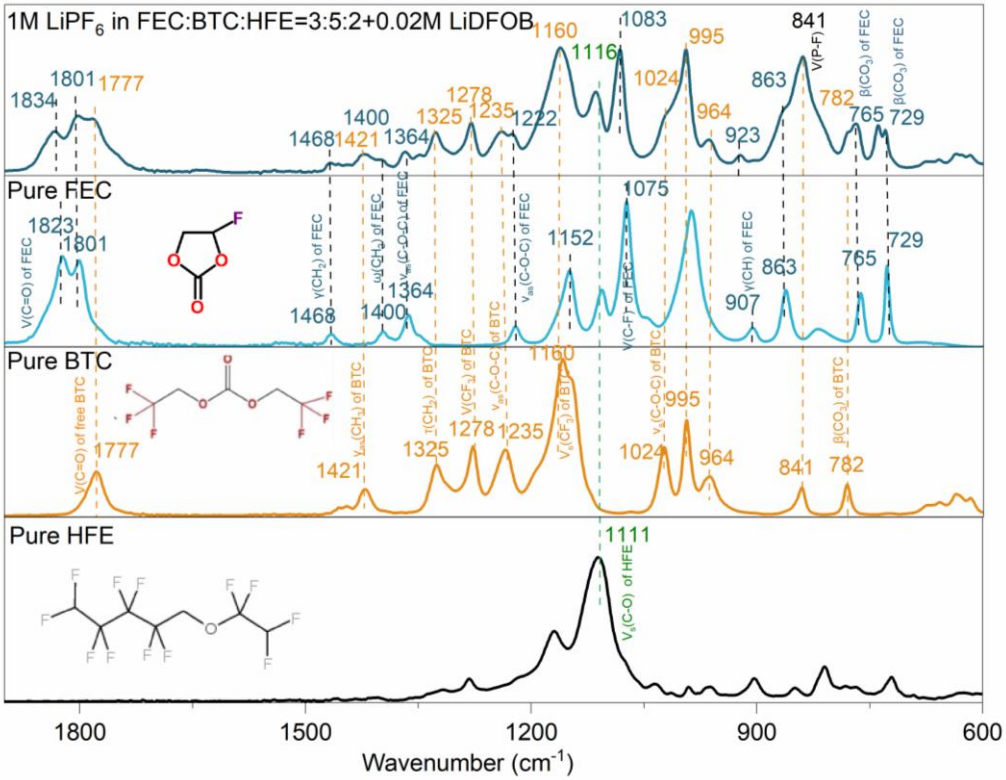

Fig. S9: Full FTIR spectra of FBH electrolyte and the corresponding pure FEC, BTC, and HFE solvents, to confirm the assignment of peak positions in the mixed solution.

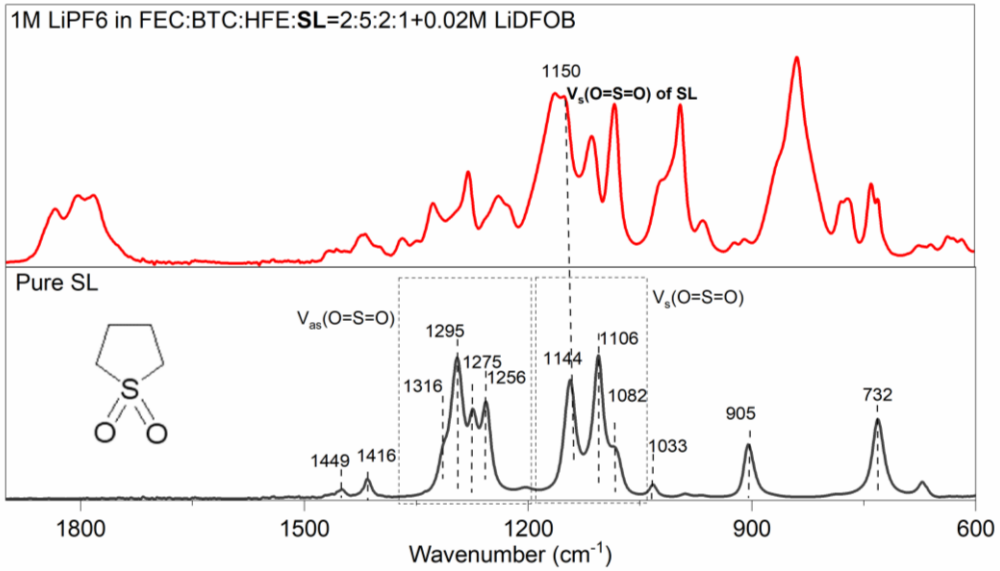

Fig. S10: Full FTIR spectra of FBH-SL electrolyte and the corresponding pure SL solvent, to confirm the assignment of peak positions in the mixed solution.

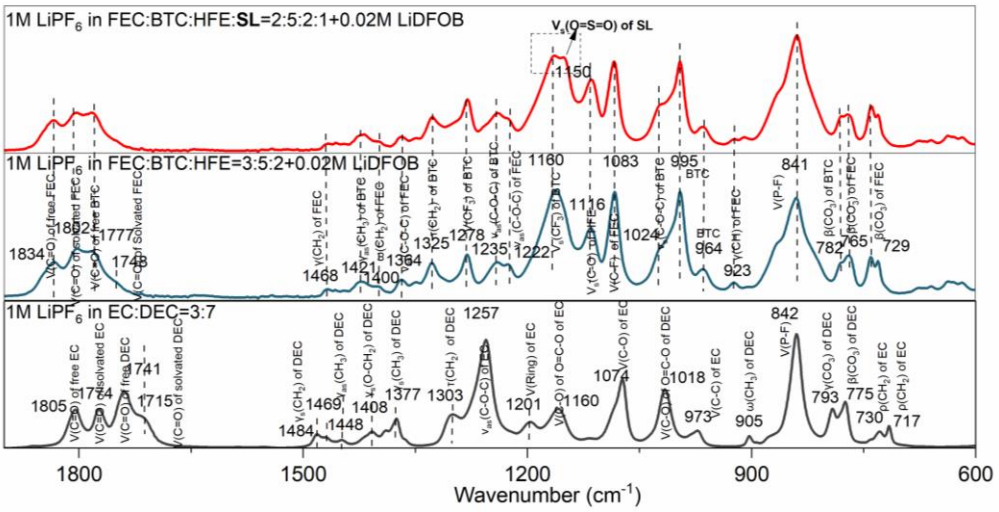

Fig. S11: Peak assignment of the three electrolytes.

The solvation structures were deconvoluted by FTIR and Raman spectra (**Fig. S8-11**, **Table S1-S2**). The spectral characteristics of free and solvated associated carbonyl groups (C=O)[3-5], observed in the range of 1670-1850 cm^{-1} for EC-DEC electrolyte and 1720-1890 cm^{-1} for fluorinated electrolytes, respectively, and the ether linkage (C-O)[6] in the region of 1130-1210 cm^{-1}, were fitted using Voigt functions (**Fig. S12a-b**).

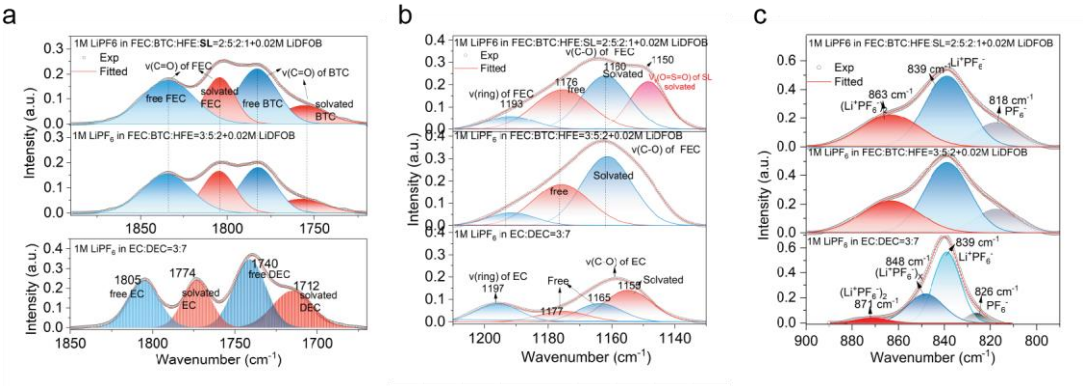

Fig. S12: Fitted FTIR spectra of solvents in different electrolytes. a, C=O regions. b, C-O regions. c, P-F regions.

It is observed that fluorinated solvents (FEC, BTC and HFE) have lower binding energy with Li^+ than non-fluorinated counterparts (EC/DEC), this is due to the strong electron-withdrawing of F atom, therefore, binding energy of FEC-Li^+ is relatively lower than EC-Li^+ in the mixture system, and this agrees well with the calculated electrostatic potential (Fig 2d).

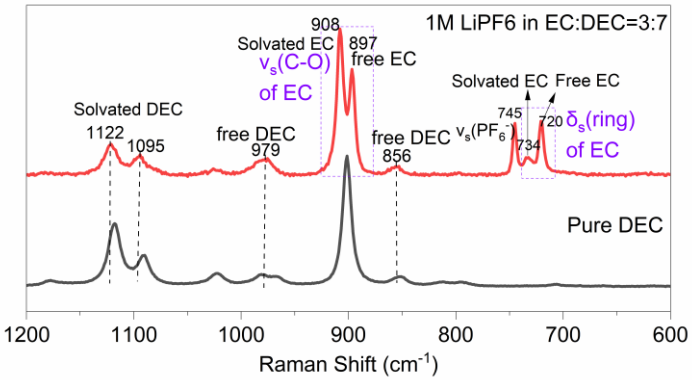

Fig. S13: Raman spectra of EC-DEC electrolyte and the corresponding pure DEC solvent, to confirm the assignment of peak positions in the mixed solution.

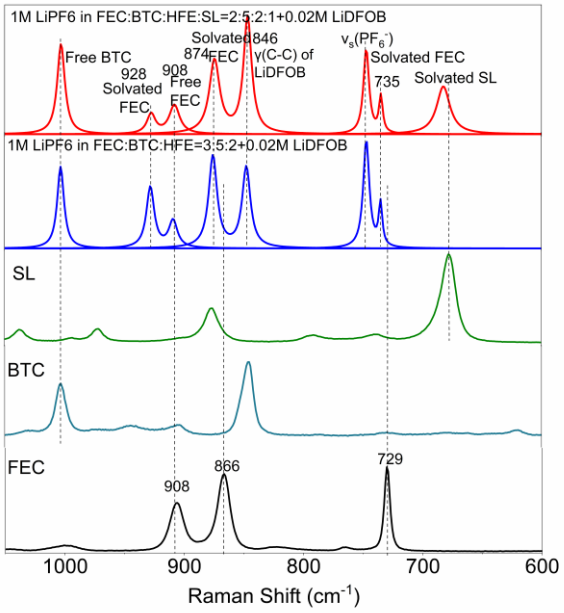

Fig. S14: Raman spectra of FBH electrolyte, HFB-SL electrolyte and the corresponding pure FEC, BTC, HFE, and SL solvent, to confirm the assignment of peak positions in the mixed solution.

Table S1 The FT-IR peak information

Number	EC-DEC		Fluorinated electrolyte		
			FBH	FBH-SL	
	Wavenumber (cm^{-1})	Band Assignment	Wavenumber (cm^{-1})	Wavenumber (cm^{-1})	Band Assignment
1	1805	ν(C=O) of free EC[3-5]	1834	1834	ν(C=O) of free FEC[7, 8]
2	1774	ν(C=O) of solvated EC[3-5]	1802	1802	ν(C=O) of solvated FEC[7, 8]
3	1741	ν(C=O) of free DEC[3-5]	1777	1777	ν(C=O) of free BTC
4	1715	ν(C=O) of solvated DEC[3-5]	1748	1748	ν(C=O) of solvated BTC
5	1484	γ_s(CH$_2$) of DEC[6]	—	—	
6	1469	γ(CH$_2$) of EC[6]	1468	1468	γ(CH$_2$) of FEC[7, 8]

7	1448	$\gamma_{as}(CH_3)$ of DEC[6]	1421	1421	$\gamma_{as}(CH_3)$ of BTC
8	1408	$\gamma_s(O\text{-}CH_2)$ of DEC[6]	1400	1400	$\omega(CH_2)$ of FEC[7, 8]
9	1377	$\gamma_s(CH_3)$ of DEC[6]	1364	1364	ν_{as}(C-O-C) of FEC[7, 8]
10	1303	$\tau(CH_2)$ of DEC [6]	1325	1325	$\tau(CH_2)$ of BTC
11	—	—	1278	1278	$\nu_{as}(CF_3)$ of BTC
12	1257	ν_{as}(C-O-C) of EC[6]	1235	1235	ν_{as}(C-O-C) of BTC
13	—	—	1222	1222	ν_{as}(C-O-C) of FEC
14	1201	ν(ring) of EC[6]	—	—	
15	1160	ν(C-O) of O=C-O of EC[6]	1160	1160	ν_s(CF3) of BTC
16	—	—	—	1150	ν_s (O=S=O) of SL
17	—	—	1116		ν_s(C-O) of HFE
18	1074	ν(C-O) of EC[9]	1083	1083	ν(C-F) of FEC[7, 8]
19	1018	ν_s(C-O) of O-C-O of DEC[9]	1024	1024	ν_s(C-O-C) of BTC
20			995	995	BTC
21	973	ν(C-C) of EC[9]	964	964	BTC
22			923	923	γ(CH) of FEC[7, 8]
23	905	$\omega(CH_3)$ of DEC[9]	863	863	
24	842	ν(P-F)[10]	841	841	P-F[10]
25			821	821	
26	793	$\beta(CO_3)$ of DEC[6]	782	782	$\beta(CO_3)$of BTC
27	775	$\beta(CO_3)$ of EC[6]	765	765	$\beta(CO_3)$ of FEC
28	730	$\rho(CH_2)$ of EC[6]	729	729	$\beta(CO_3)$ of FEC
29	717	$\rho(CH_2)$ of EC[6]			

Note:

ν_s	symmetrical stretching virbration
ν_{as}	asymmetrical stretching virbration
β	in-plane bending virbration
γ	out-of plane bending virbration
δ_s	symmetrical deformation virbration
δ_{as}	asymmetrical deformation virbration
δ	scissoring virbration
ρ	rocking virbration
ω	wagging virbration
τ	twisting （torsion） virbration

Table S2 The Raman peak information

Number	EC-DEC		Fluorinated electrolyte		
			FBH	FBH-SL	
	Raman Shift (cm^{-1})	Band Assignment	Wavenumber (cm^{-1})	Wavenumber (cm^{-1})	Band Assignment
1	—	—	—	682	Solvated SL
2	720	δ_s(ring) of free EC[11] γ(ring) of C=O of EC[12]	—	—	
3	734	δ_s(ring) of solvated EC[11]	734	734	δ_s(ring) of solvated FEC[13]
4	745	$\nu_s(PF_6^-)$ of $LiPF_6$[12]	846	846	γ(C-C) of LiDFOB[14]
5	897	ν_s(C-O) of free EC[11] ring breath of free EC[12]	874	874	Solvated FEC[13]
6	908	ν_s(C-O) of solvated EC[11] ring breath of solvated	908	908	Free FEC[13]

	EC[12]			
7		928	928	Solvated FEC[13]
8		1003	1003	Free BTC

Table S3: Fitting parameters of the C=O stretching modes in the experimental FTIR Spectra.

	Peak belongings	Peak position (cm^{-1})	FWHM	Area	Area percentage (%)
EC-DEC	Free EC	1805.2686	22.907607	5.826827	23.25595884
	Solvated EC	1772.8611	20.041345	5.0817208	20.28210032
	Free DEC	1741.1121	22.99466	8.4834275	33.85894944
	Solvated DEC	1715.3342	28.438463	5.6632231	22.60298501
FBH	Free FEC	1837.2516	28.099477	4.9871071	26.44190435
	Solvated FEC	1804.5229	28.099477	6.3277273	33.54994322
	Free BTC	1779.9498	28.099476	5.7865686	30.6806913
	Solvated BTC	1752.4857	28.099473	1.7592122	9.327435683
FBH-SL	Free FEC	1834.1341	35.484456	6.6228315	34.3726966
	Solvated FEC	1804.5187	20.170594	3.9872482	20.69393924
	Free BTC	1783.0913	27.182525	6.4130622	33.28398756
	Solvated BTC	1756.0774	31.068138	2.244568	11.64937608

Table S4: Fitting parameters of the C-O stretching modes in the experimental FTIR Spectra.

	Peak belongings	Peak position (cm^{-1})	FWHM	Area	Area percentage (%)
EC-DEC	Free EC (Ring)	1195.8399	16.547486	1.4292384	21.94
	Free EC (C-O)	1163.7633	16.851786	2.3946146	36.76
	Solvated EC (C-O)	1154.854	18.023645	2.6893021	41.29
FBH	Free FEC (Ring)	1191.3908	17.821044	1.086333	8.06
	Free FEC (C-O)	1175.8938	20.835351	4.1034785	30.44
	Solvated FEC (C-O)	1161.4351	18.857528	6.2118217	46.09
FBH-SL	Free FEC (Ring)	1191.6967	17.76157	1.1071539	8.62
	Free FEC (C-O)	1175.5255	21.219532	4.0220859	31.32
	Solvated FEC (C-O)	1161.9904	17.857904	4.5583027	35.50
	Solvated SL	1148.4754	13.850336	3.1586475	24.60

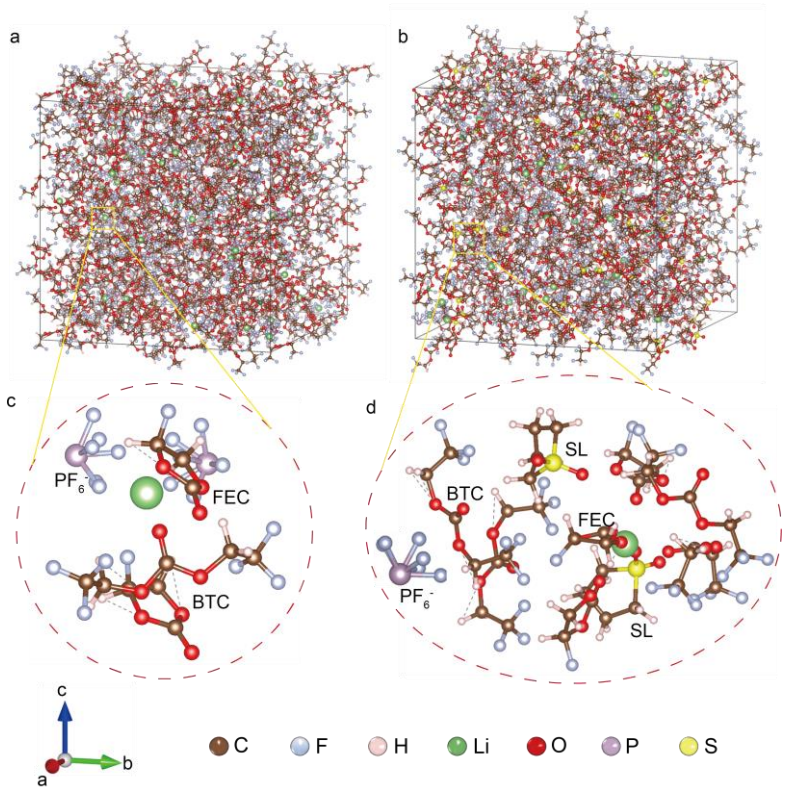

Fig. S15. Solvation structure based on molecular dynamics simulations. (a-b) system structure of FBH electrolyte (a) and FBH-SL electrolyte (b); (c-d) local structure of FBH electrolyte (c) and FBH-SL electrolyte (d).

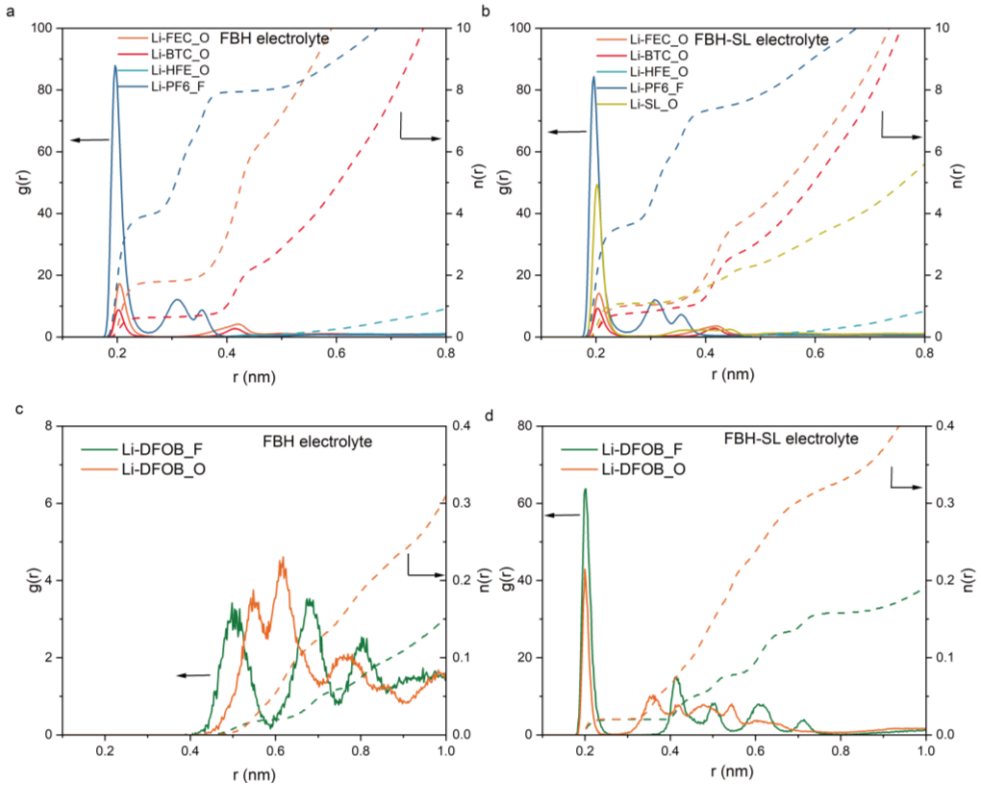

Figure S16. Radial distribution function (RDF) and coordination number (CN) of Li with solvents and anion for (a) FBH, (b) FBH-SL. RDF and CN of Li with O atoms and F atoms in DFOB for (c) FBH, (d) FBH-SL.

For both electrolytes, the first solvation radius for each solvent (FEC, BTC, and SL) was ~0.2 nm, the HFE solvent hardly participates in coordination, and PF_6^- occupied both the first and the second solvation shell with the coordination numbers dominated in the second shell. In the FBH electrolyte, FEC was the dominated solvent in the first Li^+ solvation shell, with a coordination number of 1.81, followed by linear fluorinated carbonate BTC (0.66) (Fig S16a). However, the Li^+ solvation structure was changed significantly with the addition of the SL cosolvent, SL strongly coordinates with Li^+ with a coordination number of 1.07, and simultaneously reduced the coordination number of FEC to ~1.01 (Fig S16b). This further evidenced that SL occupies the coordination site of the main solvents, which is well agreeing with the FTIR and Raman result (Fig.2 a-c).

Furthermore, the cosolvent SL also promotes the additive anion $DFOB^-$ to coordinate with Li^+, evidenced by the coordination number of $DFOB^-$ in FBH-SL electrolyte is relative higher than that in FBH electrolyte, and the radial distribution functions (RDFs) (g(r)) of FBH-SL electrolyte is much stronger than that of FBH electrolyte (Fig S16c-d). This MD simulation results well coincides with the Raman characterization (Fig 2c).

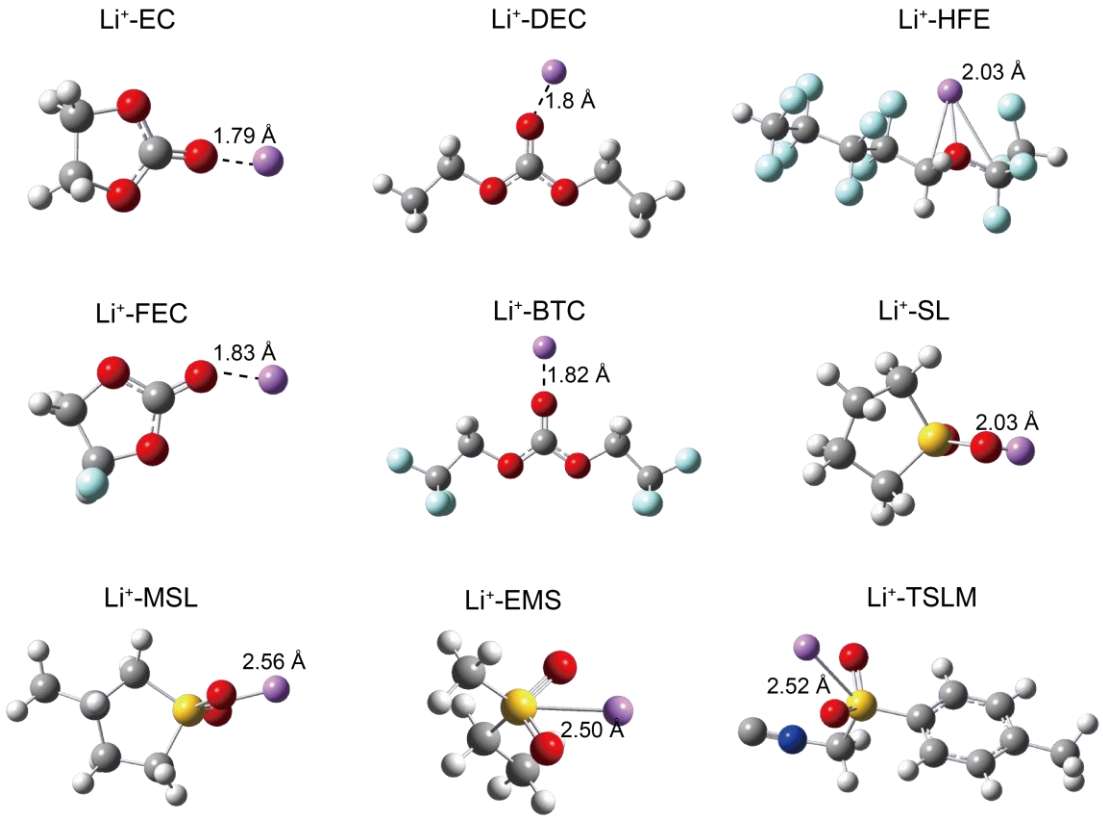

Fig. S17: Binding energy of Li^+ with carbonated solvents and the possible sulfone solvents.

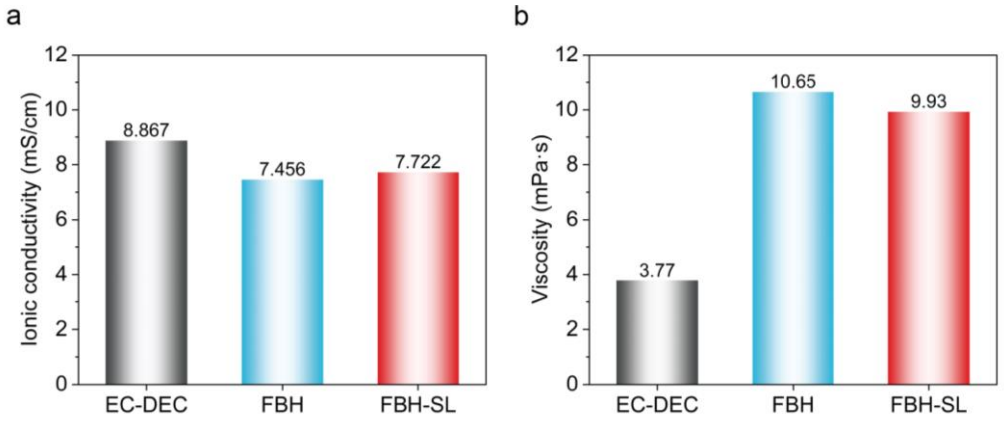

Fig. S18: Physical properties of three electrolytes. a, Ionic conductivity. b, Viscosity.

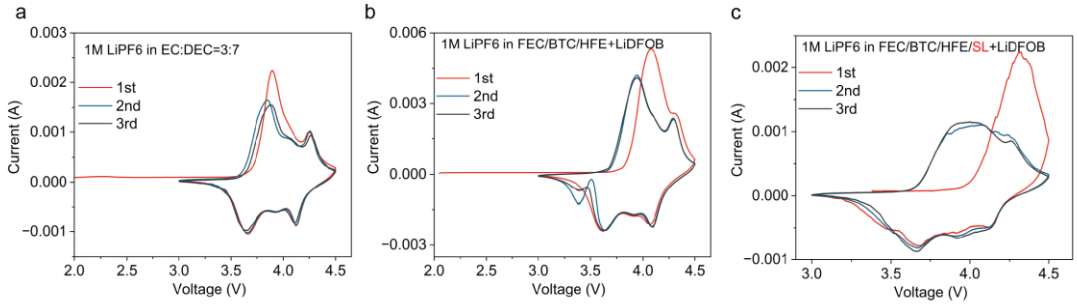

Fig. S19: The first three CV cycles of the NCM811/Li cells with different electrolytes.

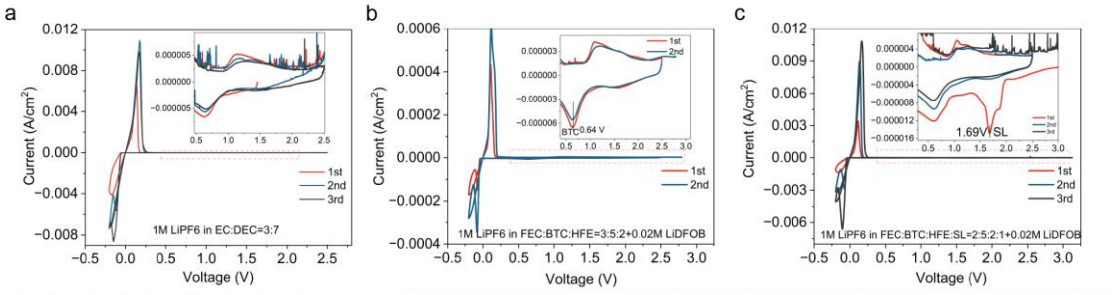

Fig. S20: The first three CV cycles of the Li/Cu cells with different electrolytes.

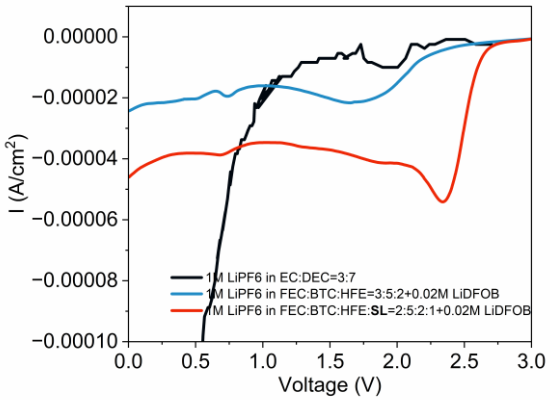

Fig. S21: Reduction LSV plots of three electrolytes in a three-electrode system, with carbon as the work electrode, lithium foil as the counter electrode and reference electrode.

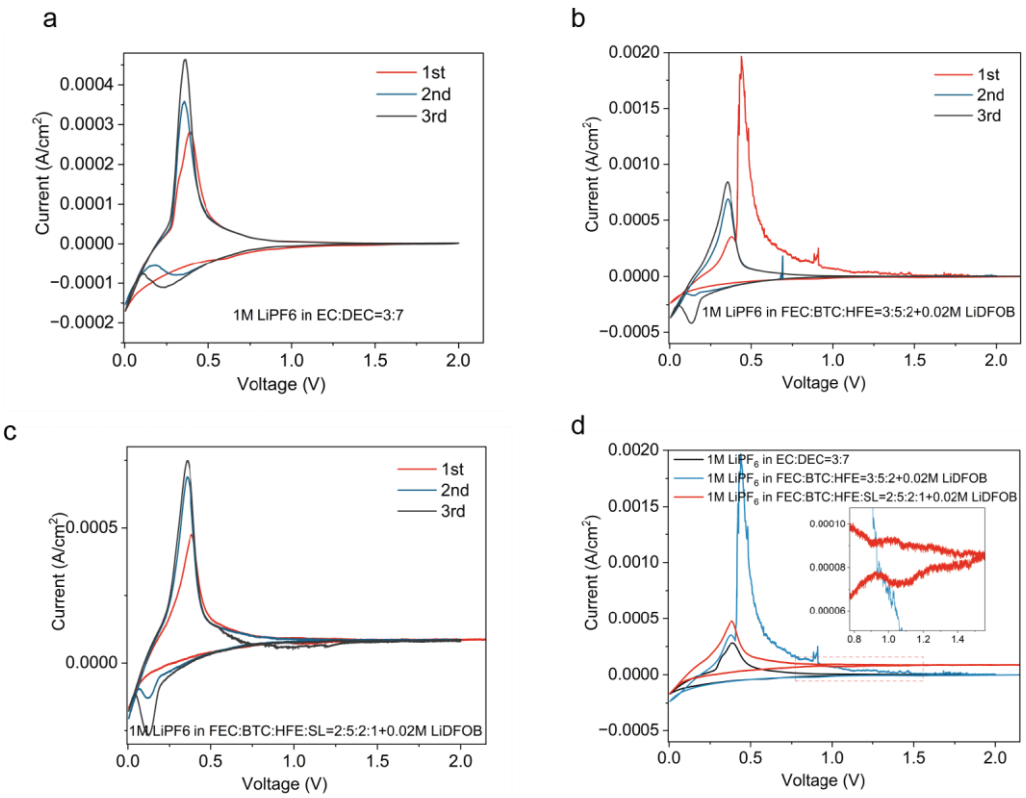

Fig. S22: CV curves of Gr/Li half cells under first 3 cycles. a, EC-DEC electrolyte. b, FBH electrolyte. c, FBH-SL. d, CV curve comparison of initial cycle for three electrolytes.

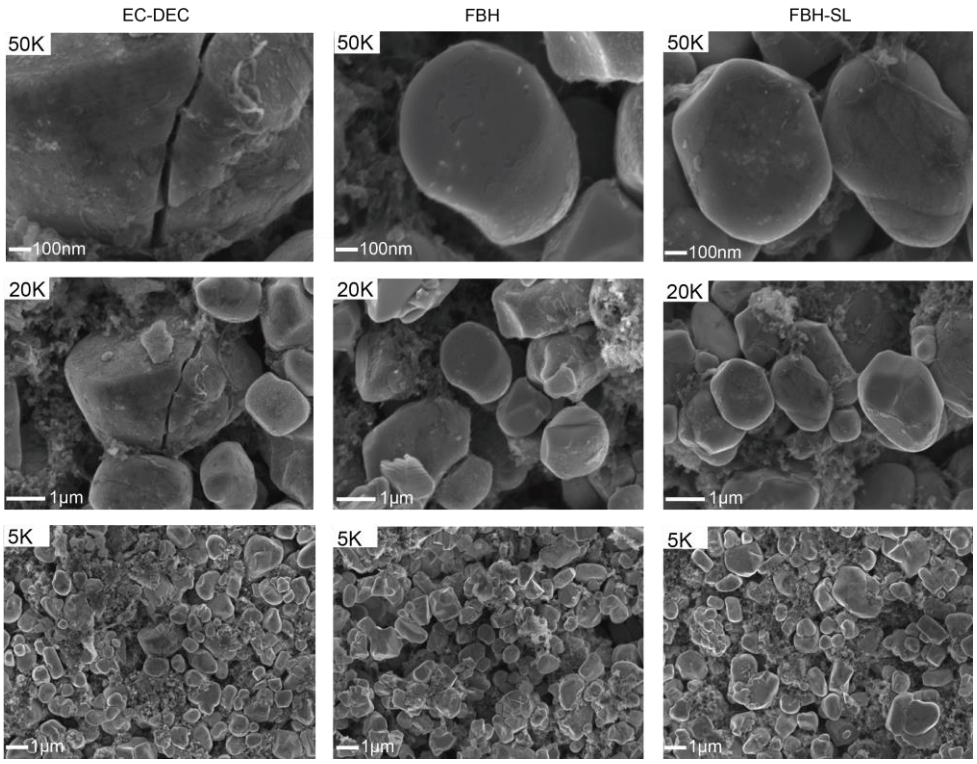

Fig. S23: SEM images of the NCM811 cathode disassembled from NCM811/Li cells after 4.7 V floating test for the three electrolytes.

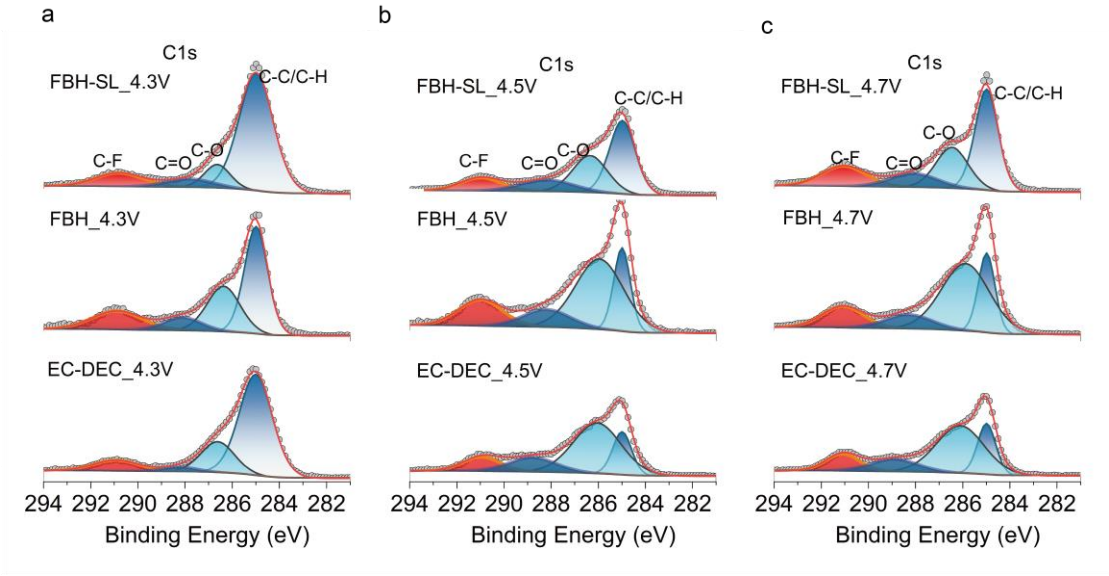

Fig. S24: C1s spectra of XPS profile of NCM811 cathode disassembled from the NCM811/Li cells after 3 formation cycles with fully charged state.

Within the C1s spectra, peaks located at ~285 eV, ~286.2 eV, ~288.5 eV, and ~290.9 eV are assigned to C-C, C-O, C=O, and C-F, respectively. In which, the C-O/ C=O components increased with the cutoff voltage increased, suggesting the main solvents trend to be severely decomposed when operation voltage rosed in the EC-DEC electrolyte (**Fig 3a, Fig S21**).

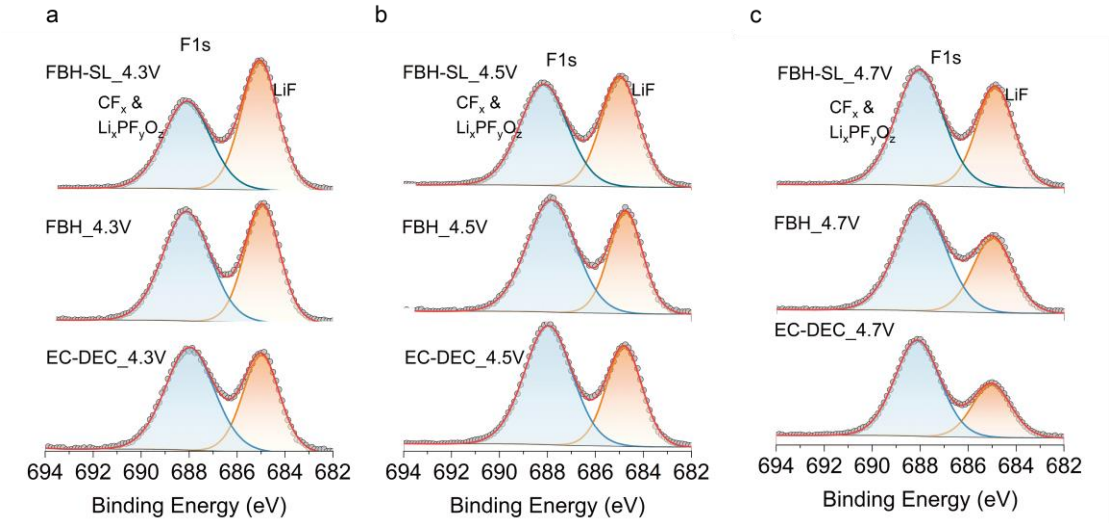

Fig. S25: F1s spectra of XPS profile of NCM811 cathode disassembled from the NCM811/Li cells after 3 formation cycles with fully charged state.

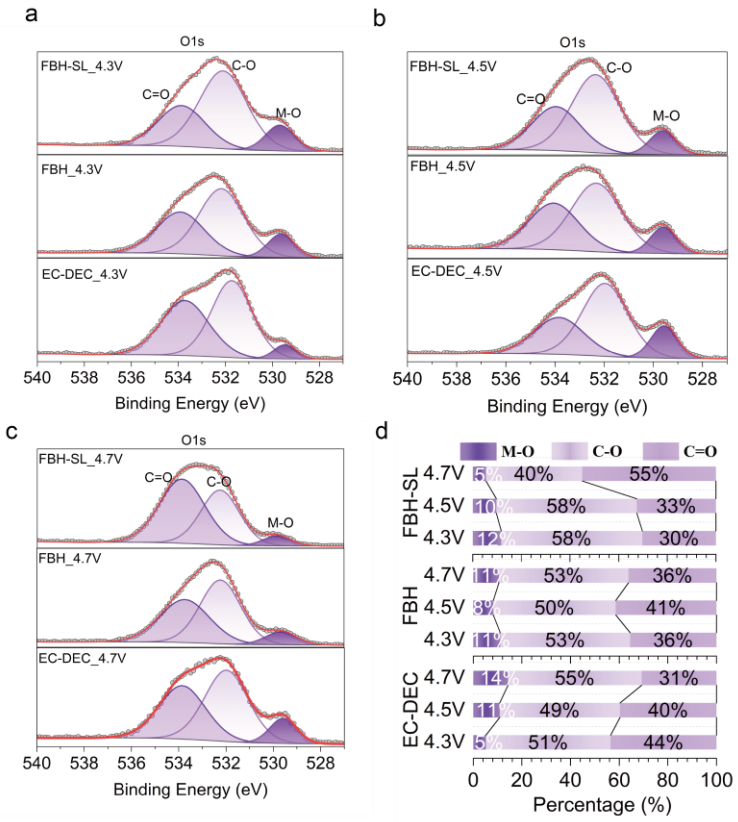

Fig. S26: O1s spectra of XPS profile of NCM811 cathode disassembled from the NCM811/Li cells after 3 formation cycles with fully charged state.

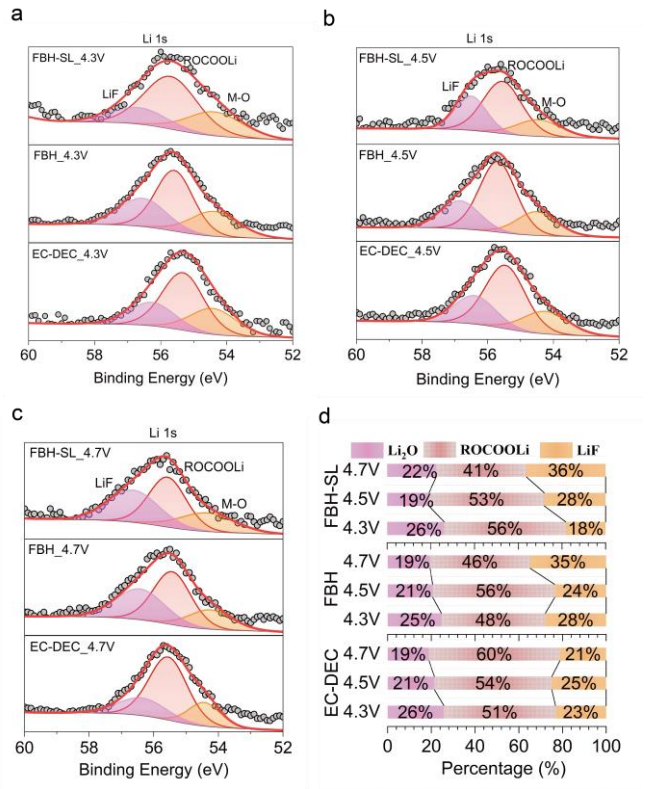

Fig. S27: Li1s spectra of XPS profile of NCM811 cathode disassembled from the NCM811/Li cells after 3 formation cycles with fully charged state.

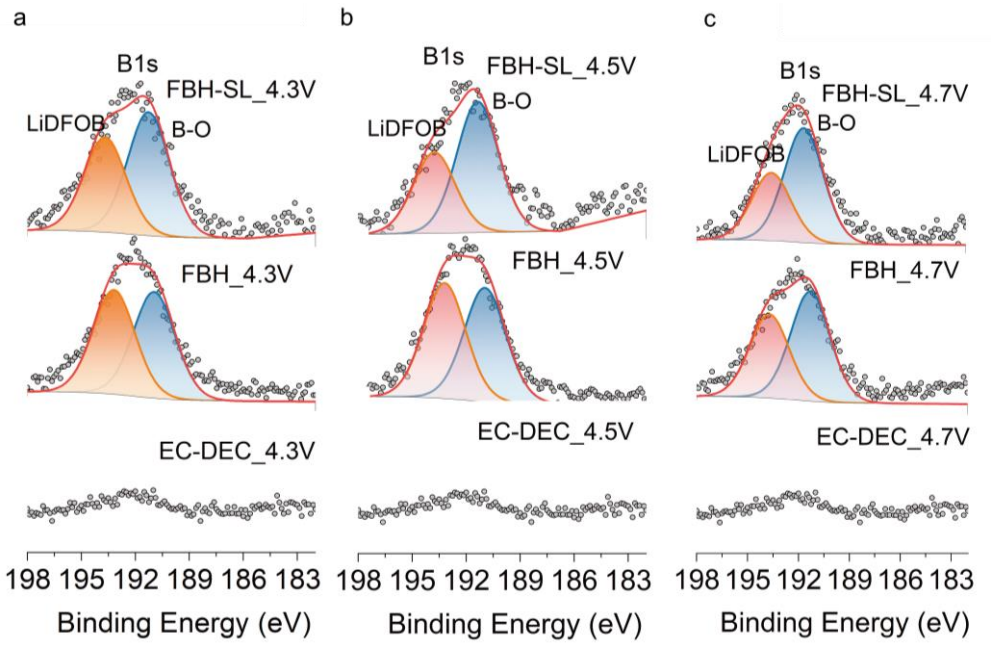

Fig. S28: B1s spectra of XPS profile of NCM811 cathode disassembled from the NCM811/Li cells after 3 formation cycles with fully charged state.

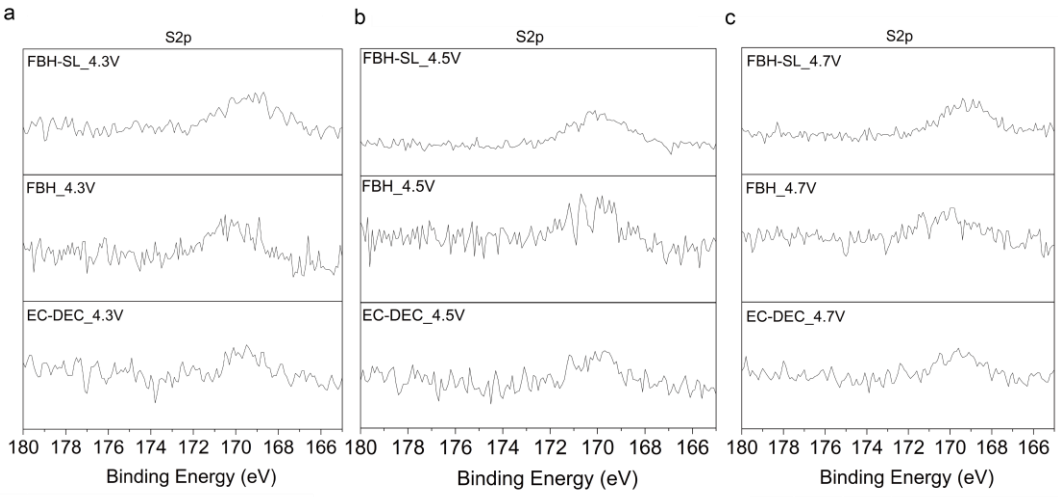

Fig. S29: S2p spectra of XPS profile of NCM811 cathode disassembled from the NCM811/Li cells after 3 formation cycles with fully charged state.

Table S5 Quantitative analysis of O 1s, F 1s and C1s XPS spectra of NCM811 electrodes with different electrolytes. The peak assignments, BE (binding energy), FWHM (full width half maximum) and At% (atomic ratio) are listed.

	Peak	Assignments	4.3 V			4.5 V			4.7 V		
			BE (eV)	FWHM (eV)	At %	BE (eV)	FWHM (eV)	At %	BE (eV)	FWHM (eV)	At %
EC-DEC	O1s	Li_2O[15]	529.48	1.1	5.16	529.59	1.34	10.81	529.56	1.26	14.20
		C=O[16, 17]	531.73	2.03	51.29	531.98	2.17	49.46	531.97	2.18	54.99
		$-CH_2CH_2O-$[15, 18]	533.72	2.40	43.55	533.85	2.32	39.73	533.84	2.40	30.81
	Li1s	Li_2O[19, 20]	54.42	1.66	25.76	54.25	1.62	21.42	54.43	1.17	18.88
		ROCOOLi[19, 20]	55.33	1.48	51.04	55.47	1.44	53.67	55.55	1.40	59.90
		LiF[19, 20]	56.26	1.64	23.20	56.40	1.48	24.91	56.37	1.75	21.22
	F1s	LiF[2, 18, 21]	685.02	1.89	32.12	684.99	1.82	41.57	685.00	1.97	36.33
		C-F, Li_xPO_yF[2, 18, 22]	688.12	2.21	67.88	687.98	2.40	58.43	687.98	2.40	63.67
	C1s	C-C[23, 24]	285.00	1.66	65.8	285.00	0.95	18.10	285.00	0.91	21.02
		C-O[15, 18]	286.61	1,69	20.62	286.05	2.40	53.62	286.12	2.40	51.65
		C=O[15, 18, 19, 22, 25]	288.22	1.76	3.37	288.78	2.40	15.78	288.91	2.40	14.02
		C-F[21, 25]	290.92	2.32	10.22	290.94	1.94	12.50	291.10	1.69	13.31
FBH	O1s	Li_2O	529.64	1.32	11.02	529.67	1.57	8.18	529.61	1.22	10.53
		C=O	532.17	2.26	53.28	532.23	2.02	50.34	532.34	2.40	53.23
		$-CH_2CH_2O-$	533.91	2.40	35.50	533.74	2.46	41.48	534.06	2.40	36.24
	Li1s	Li_2O	54.38	1.71	24.65	54.51	1.44	20.60	54.24	1.58	19.37
		ROCOOLi	55.59	1.35	47.51	55.70	1.30	55.82	55.43	1.37	45.79
		LiF	56.55	1.68	27.84	56.85	1.39	23.57	56.43	1.79	34.84
	F1s	LiF	684.73	1.66	38.43	684.94	1.74	44.41	684.80	1.77	38.43
		$C-F_x$ & Li_xPO_yF	687.83	2.40	61.57	688.11	2.32	55.59	687.96	2.36	61.57
	C1s	C-C	285.00	1.16	45.57	285.00	0.83	20.28	285.00	0.83	21.41
		C-O	286.37	1.65	27.54	285.96	2.40	49.82	285.89	2.40	52.60
		C=O	288.11	1.91	9.3	288.21	2.40	12.75	288.31	2.40	14.71
		C-F	290.89	2.45	17.58	291.00	2.20	17.15	291.09	2.09	11.29

FBH-SL	**O1s**	**Li_2O**	529.69	1.44	11.67	529.61	1.25	9.66	529.83	1.40	5.41
		C-O	532.10	2.38	58.00	532.35	2.32	57.74	532.25	1.92	39.62
		C=O	533.86	2.36	30.33	533.96	2.32	32.60	533.86	2.27	54.97
	Li1s	**Li_2O**	54.37	1.95	26.12	54.45	1.57	19.10	54.35	1.99	22.43
		ROCOOLi	55.70	1.89	55.57	55.55	1.39	52.77	55.58	1.37	41.23
		LiF	56.66	1.98	18.30	56.51	1.12	28.13	56.63	1.86	36.34
	F1s	**LiF[18, 21]**	684.97	1.87	46.18	685.06	1.83	53.87	684.89	1.84	40.56
		C-F_x & Li_xPO_yF	688.15	2.34	53.82	688.09	2.30	46.13	688.05	2.33	59.44
	C1s	**C-C**	285.00	1.72	70.48	285.00	1.30	43.62	285.00	1.16	44.52
		C-O	286.64	1.30	10.69	286.36	1.73	29.25	286.47	1.61	25.26
		C=O	287.81	2.40	7.24	288.19	2.50	14.53	288.09	2.40	12.79
		C-F	290.81	2.40	11.58	290.98	2.07	12.60	291.06	2.24	17.41

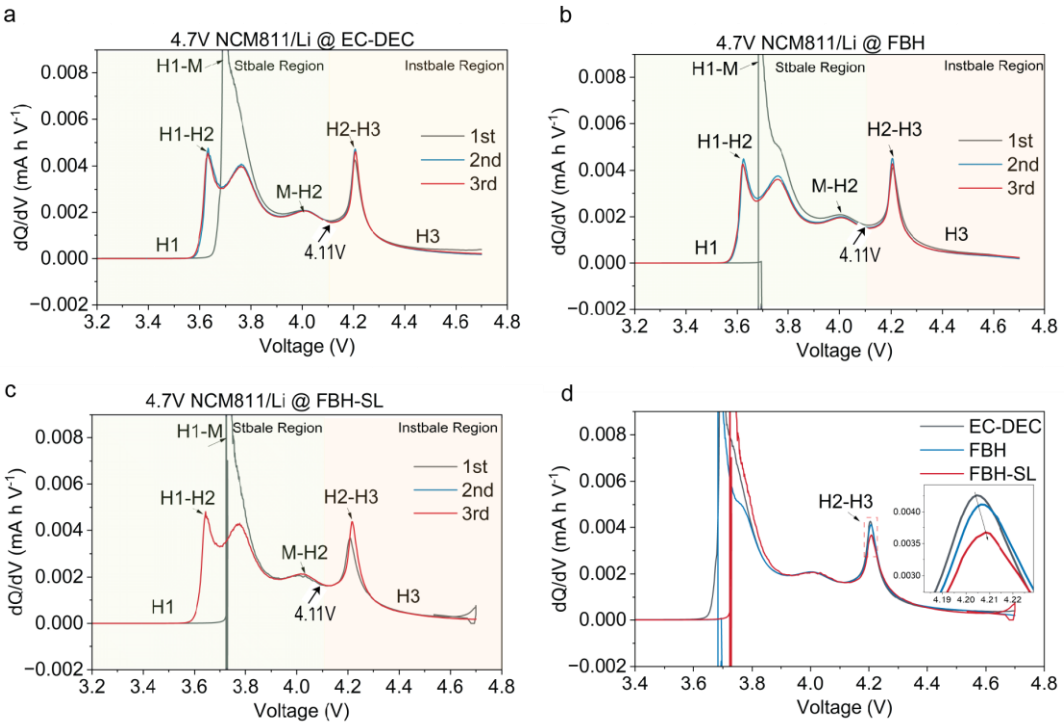

Fig. S30: a-c, Differential capacity dQ/dV plots for first three cycles of the NCM cathode with (a) EC-DEC electrolyte, (b) FBH electrolyte, and (c) FBH-SL electrolyte. d, The comparison of initial dQ/dV plot for the three electrolytes.

Depending on the cutoff voltage, the full profile can be split into stable (green) and unstable (red) regions. When the voltage is above 4.11V, the electrode undergoes the H2-H3 transition, accompanied by lattice oxygen reduction. This transition induces the lattice collapse and is considered harmful for maintaining the reversible storage capacity. Based on theoretical and experimental studies, the lattice collapse of Ni-rich NCMs is linked with c-axis lattice shrinkage during the H2-to-H3 phase transition. The c-axis parameter is related to the distance between the Li layers in the electrode material.

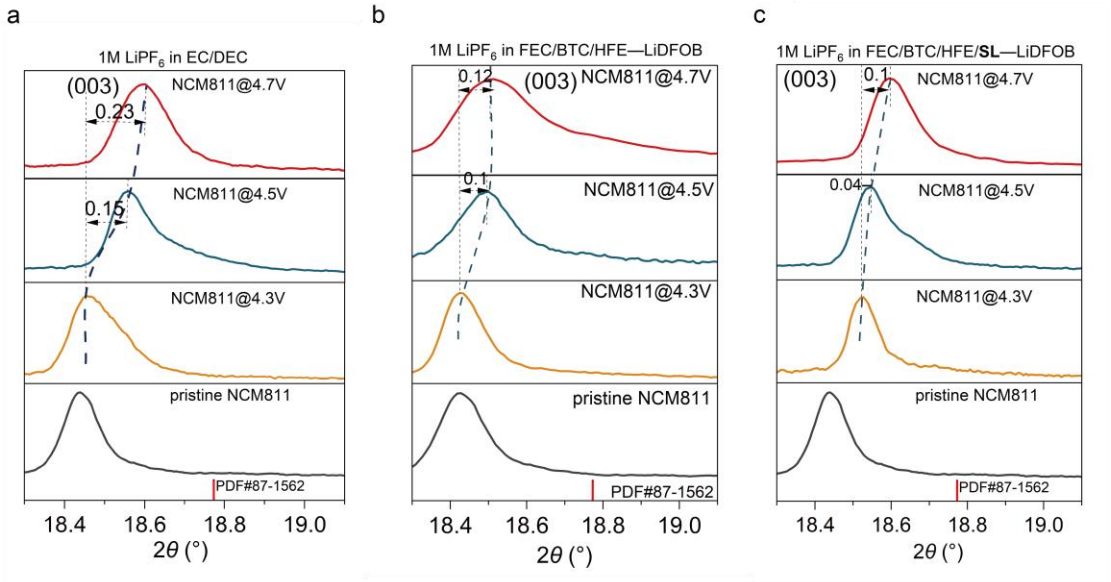

Fig. S31: (003) plane displacement of NCM811 cathode after 100 cycles under different cutoff voltage with EC-DEC electrolyte (a), FBH electrolyte (b), and FBH-SL (c). The cell was disassembled at fully discharged state.

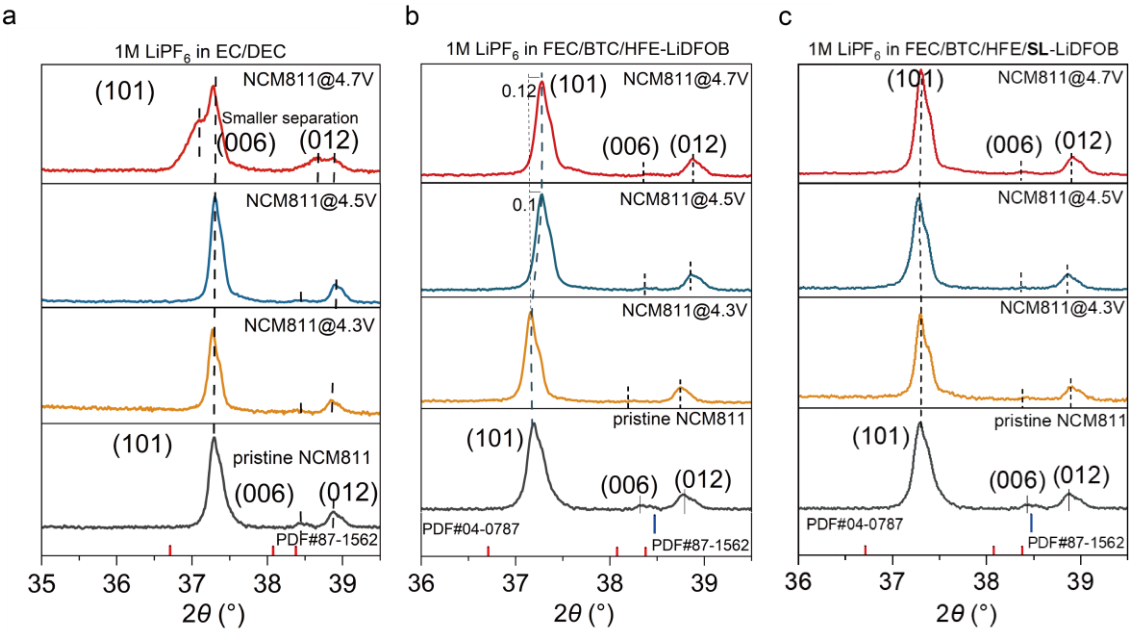

Fig. S32: (101) plane displacement and (006)/(012) separation of NCM811 cathode after 100 cycles under different cutoff voltage with EC-DEC electrolyte (a), FBH electrolyte (b), and FBH-SL (c). The cell was disassembled at fully discharged state.

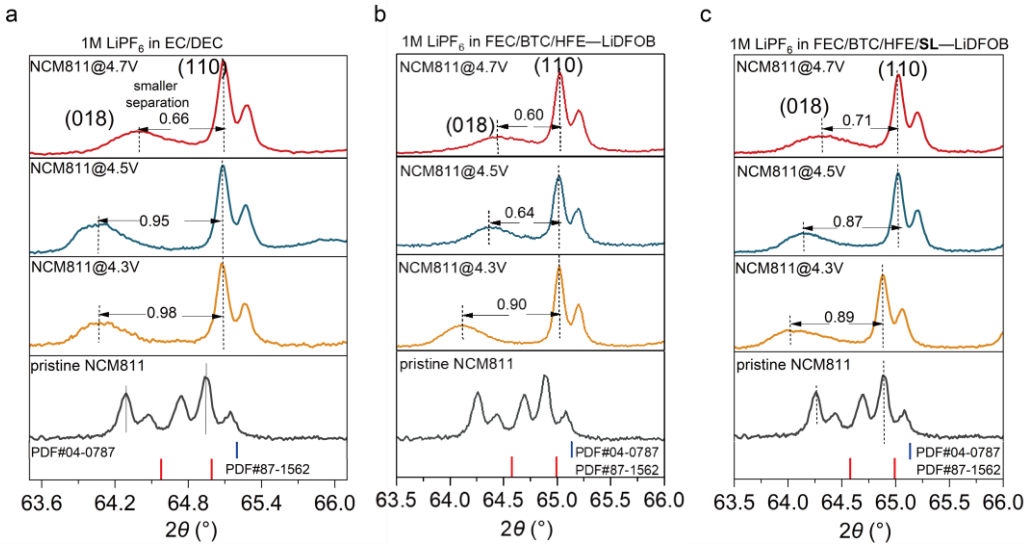

Fig. S33: (018)/(110) separation of NCM811 cathode after 100 cycles under different cutoff voltage with EC-DEC electrolyte (a), FBH electrolyte (b), and FBH-SL (c). The cell was disassembled at fully discharged state.

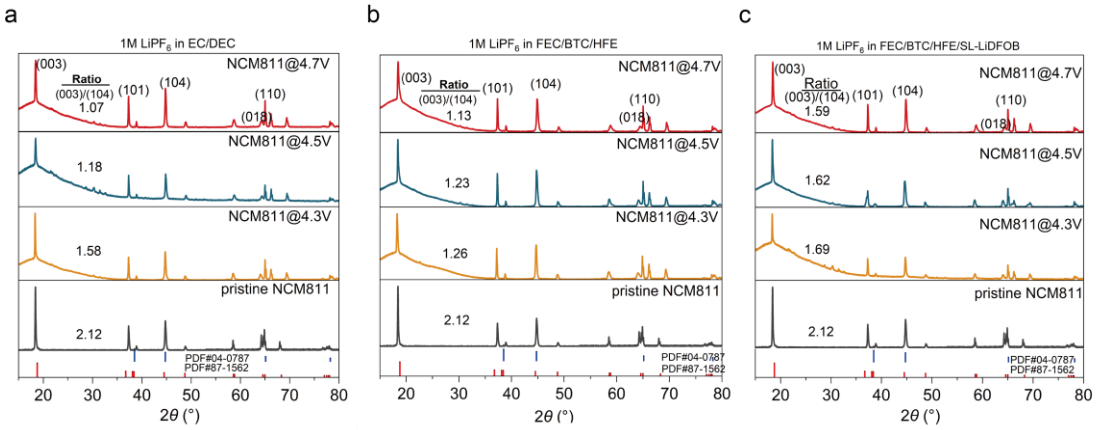

Fig. S34: Full XRD pattern and the calculated I(003)/I(104) of NCM811 cathode after 100 cycles under different cutoff voltage with EC-DEC electrolyte (a), FBH electrolyte (b), and FBH-SL (c). The cell was disassembled at fully discharged state.

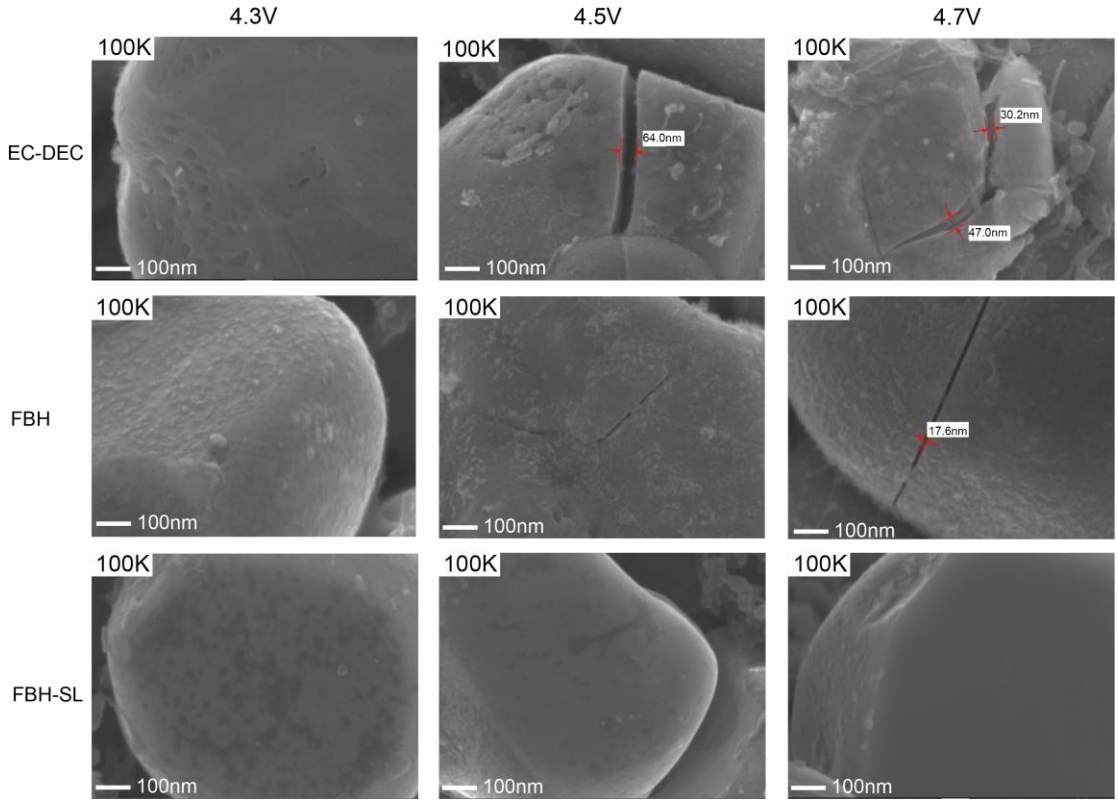

Fig. S35: 100K SEM images of the fully delithiated NCM811 cathode after 100 cycling with EC-DEC electrolyte, FBH electrolyte, and FBH-SL electrolyte with 4.7V.

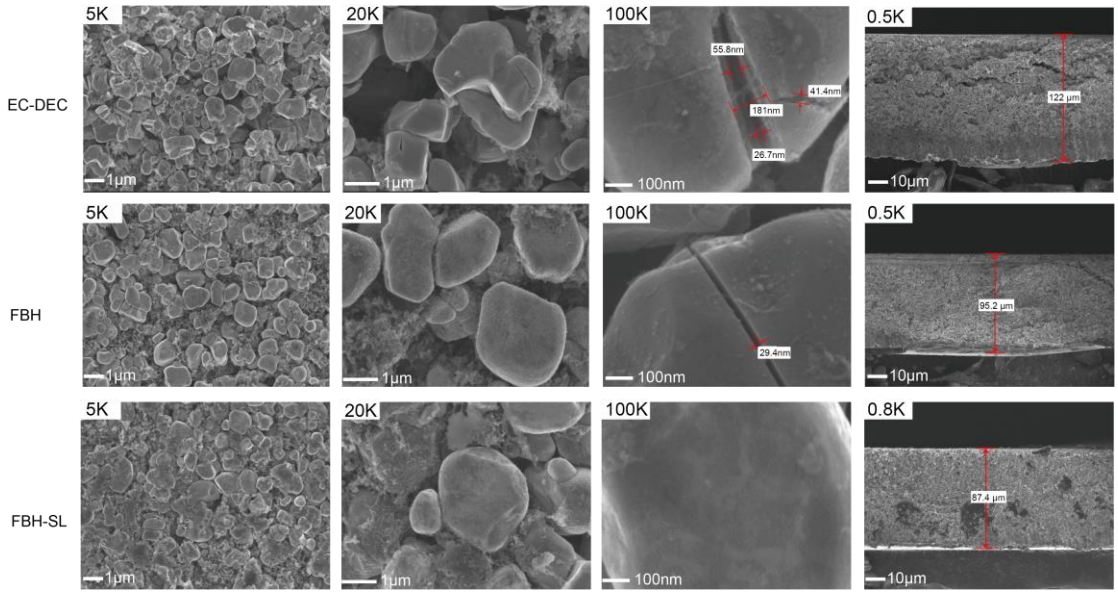

Fig. S36: 5K/20K/100K SEM images and cross-sectional images of the fully delithiated NCM811 cathode after 100 cycling with EC-DEC electrolyte, FBH electrolyte, and FBH-SL electrolyte with 4.7V.

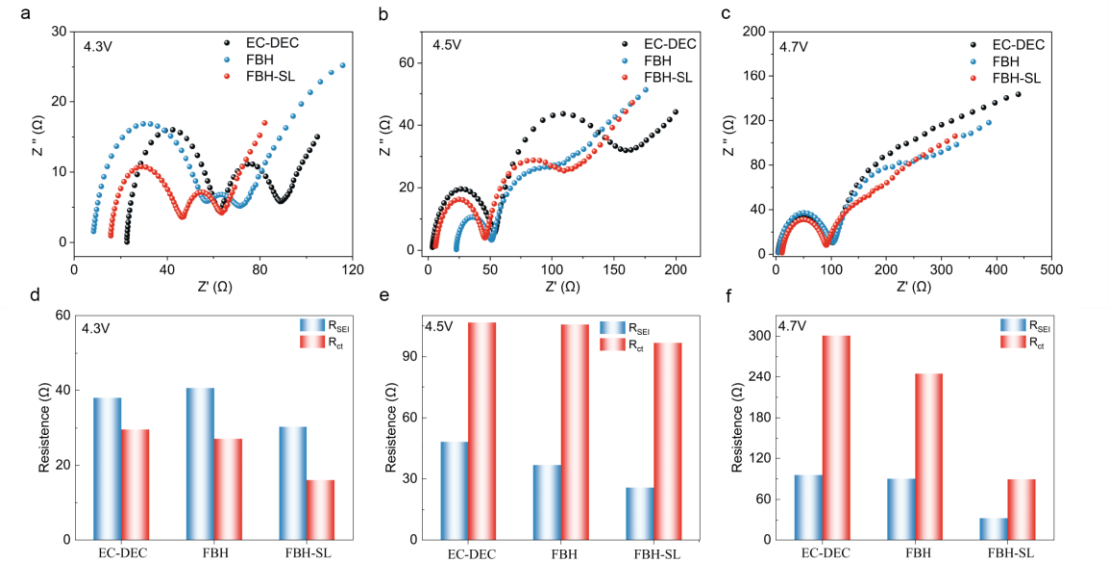

Fig. S37: Electrochemical impedance spectra (EIS) of fully charged NCM811/Li cells with different electrolytes for 3 cycles under different cutoff voltage.

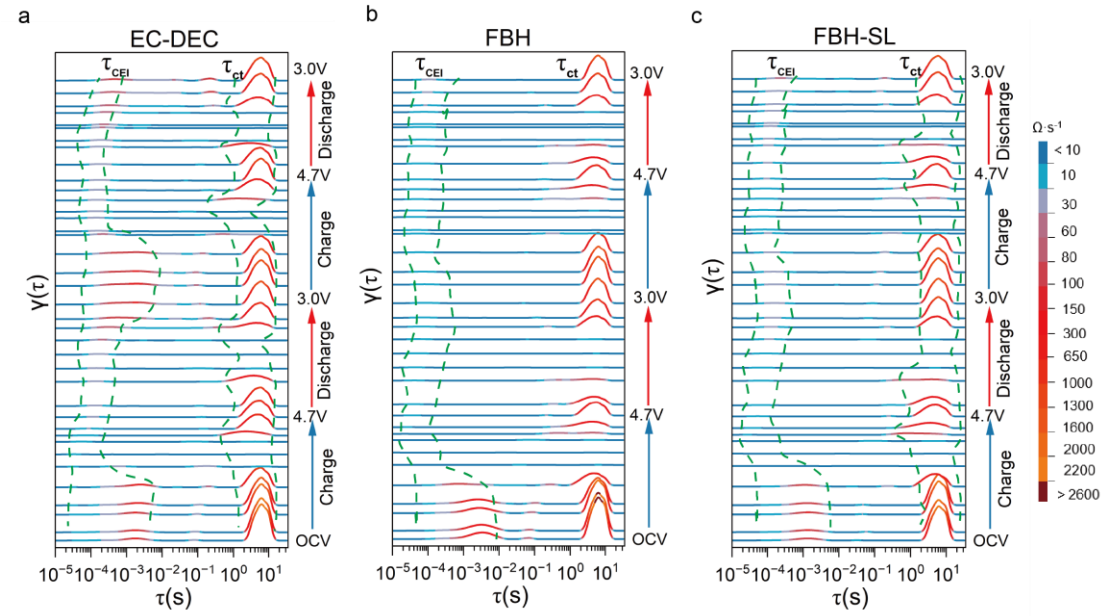

Fig. S38: Distribution of relaxation times (DRT) plot derived from in-situ EIS of NCM811/Li cells with different electrolytes for 3 formation cycles under cutoff voltage of 4.7V. a, EC-DEC electrolyte. b, FBH electrolyte. c, FBH-SL electrolyte.

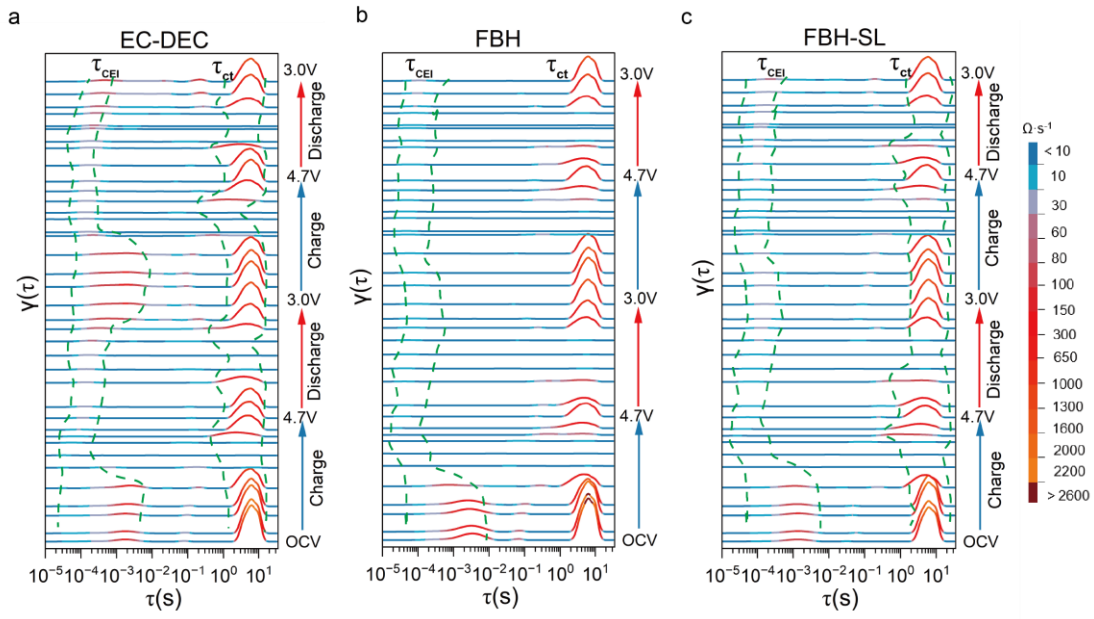

Fig. S39: Fitting impedances versus voltage profiles for the in-situ EIS data of CEI film impedance R_{CEI} (a) and charge transfer impedance R_{ct}.

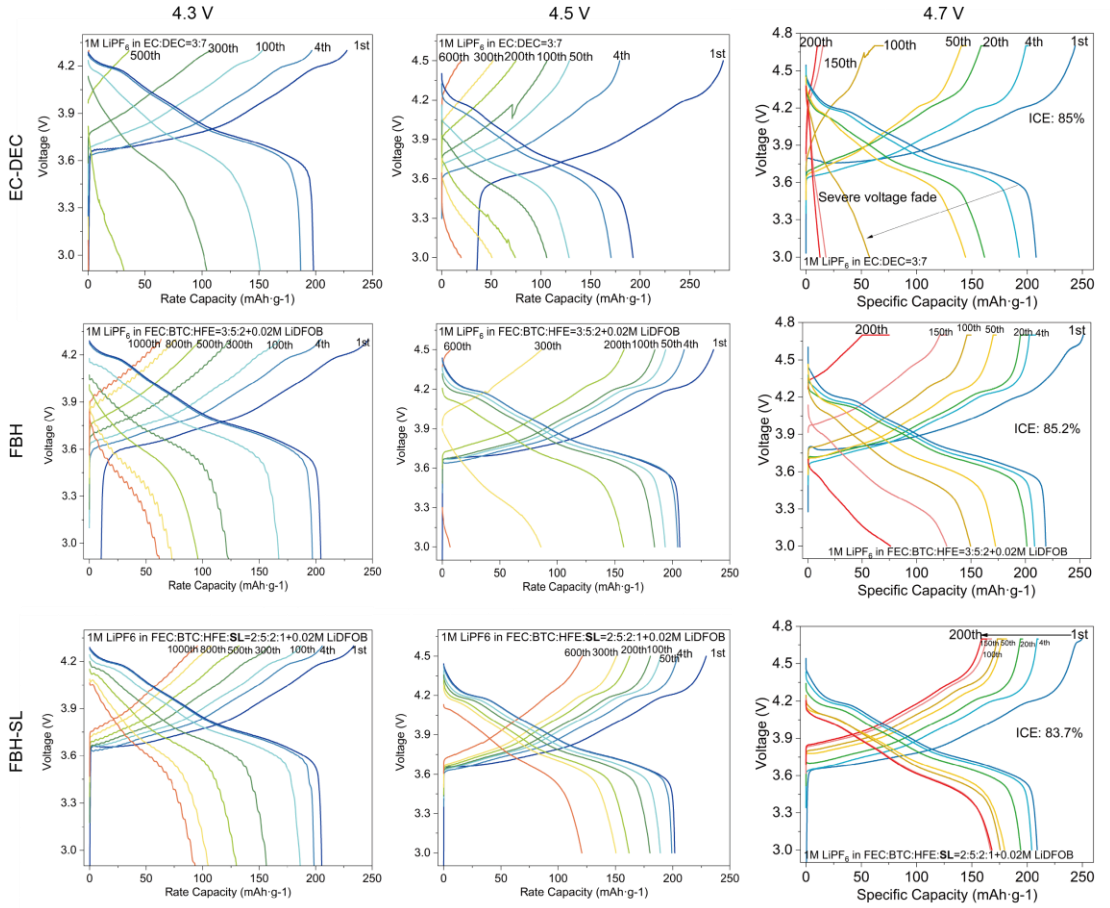

Fig. S40: Charge and discharge profiles under 4.3V, 4.5V and 4.7V with EC-DEC electrolyte, FBH electrolyte, and FBH-SL electrolyte.

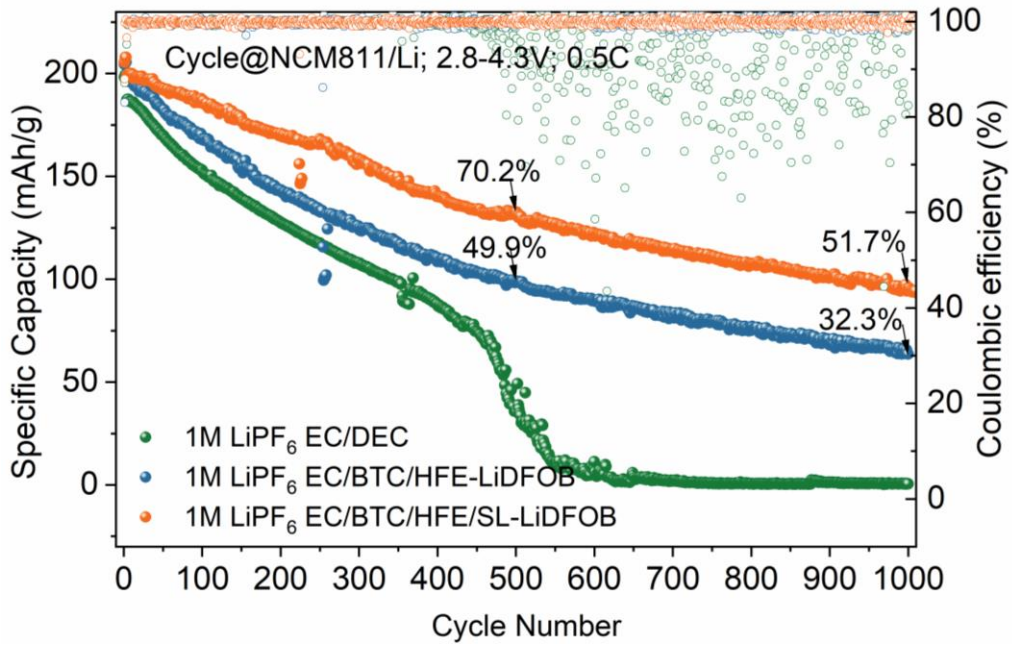

Fig. S41: Cycling behavior of NCM811/Li cell with different electrolytes under 4.3V

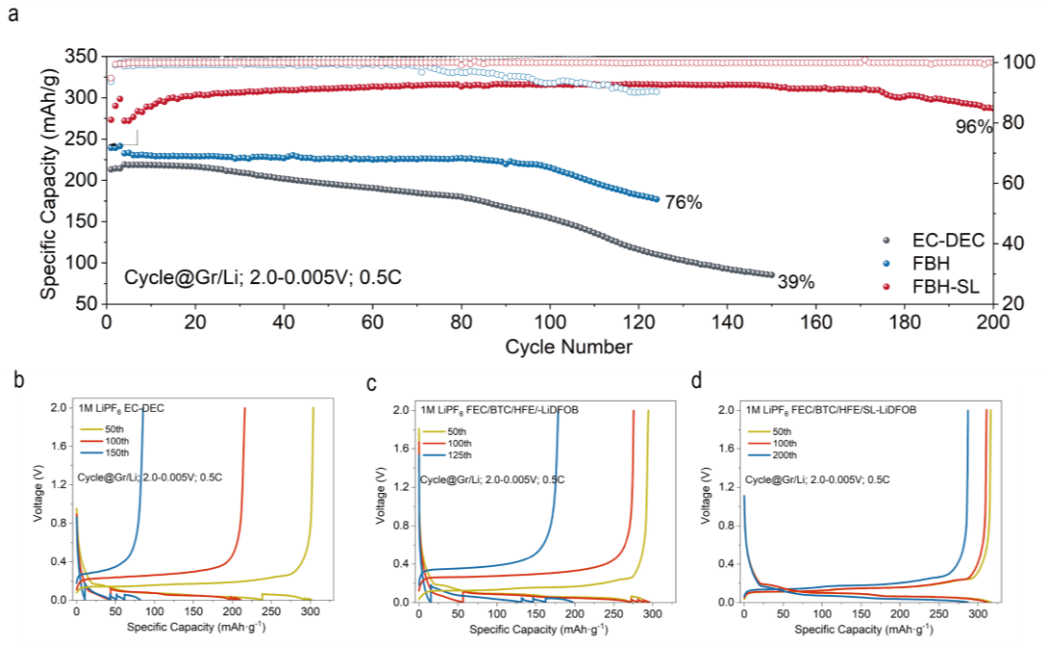

Fig. S42: Cycling performance of graphite/Li cells. a, the long cycling behavior. b-d, the charge and discharge profiles of EC-DEC electrolyte (b), FBH electrolyte (c), and FBH-SL electrolyte (d).

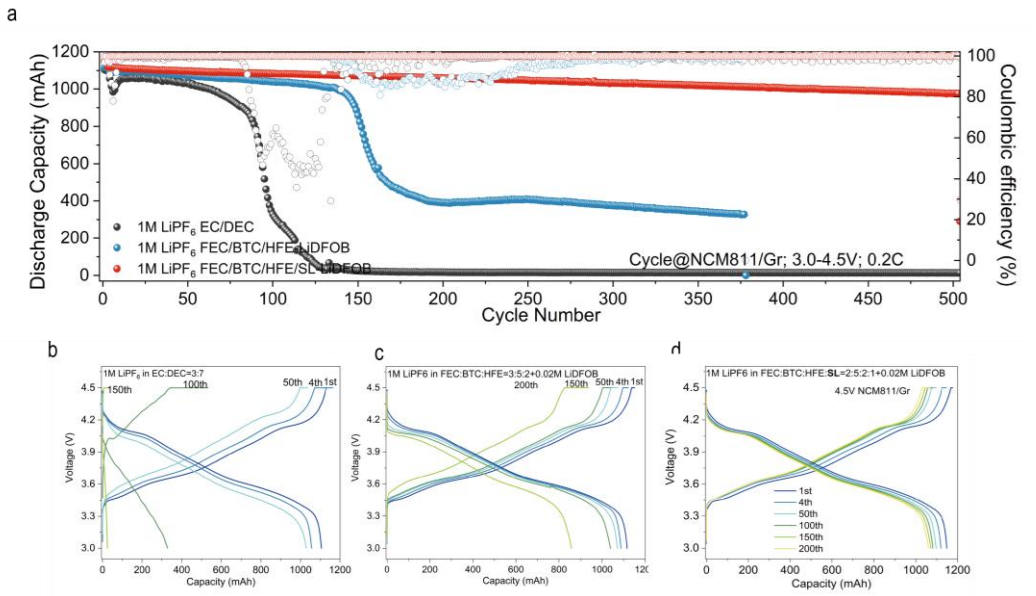

Fig. S43: Cycling performance comparison of NCM811/Gr pouch cells under 4.5V. a, the long cycling behavior. b-d, the charge and discharge profiles of EC-DEC electrolyte (b), FBH electrolyte (c), and FBH-SL electrolyte (d).

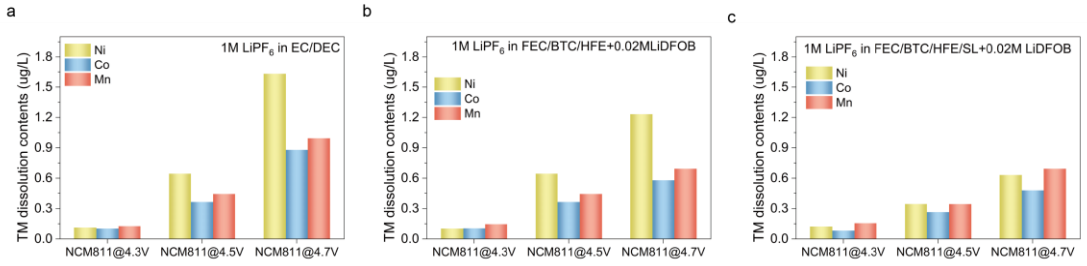

Fig. S44: TM dissolutions of the Li anode disassembled from NCM811/Li cell after 100 cycles with three different electrolytes.

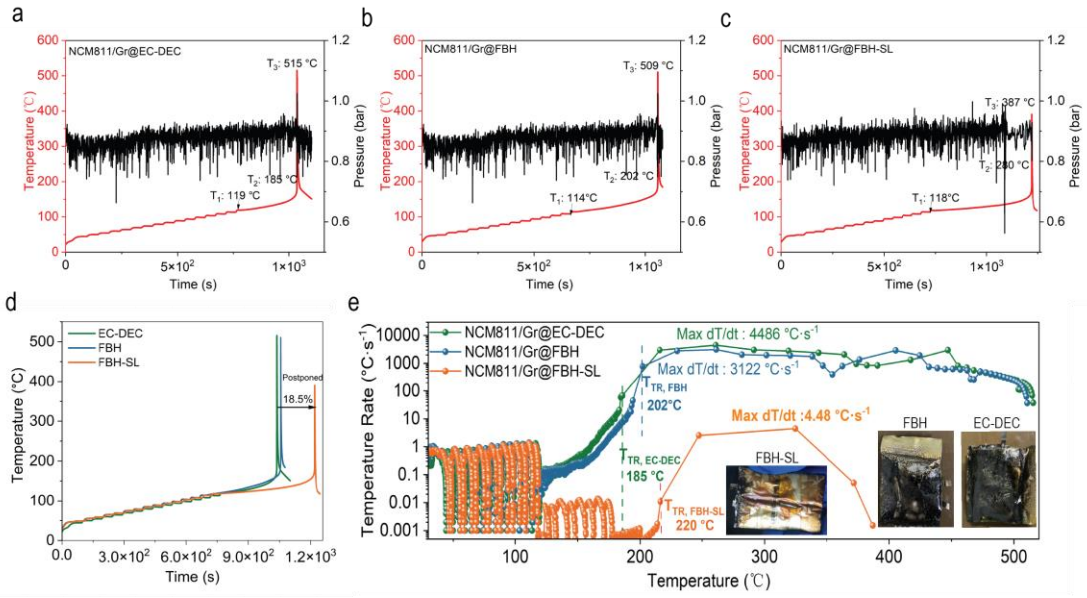

Fig. S45: ARC test of NCM811/Gr pouch cells with different electrolytes.

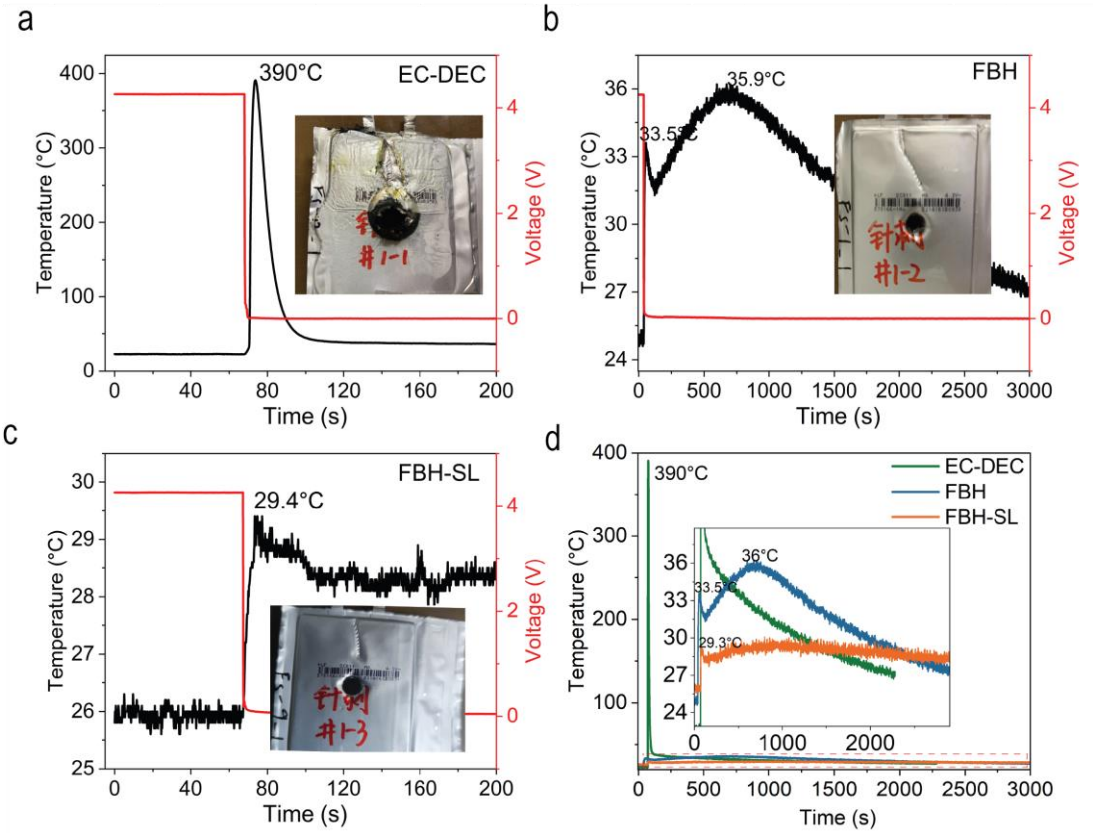

Fig. S46: Nail penetration of NCM811/Gr pouch cells with different electrolytes.

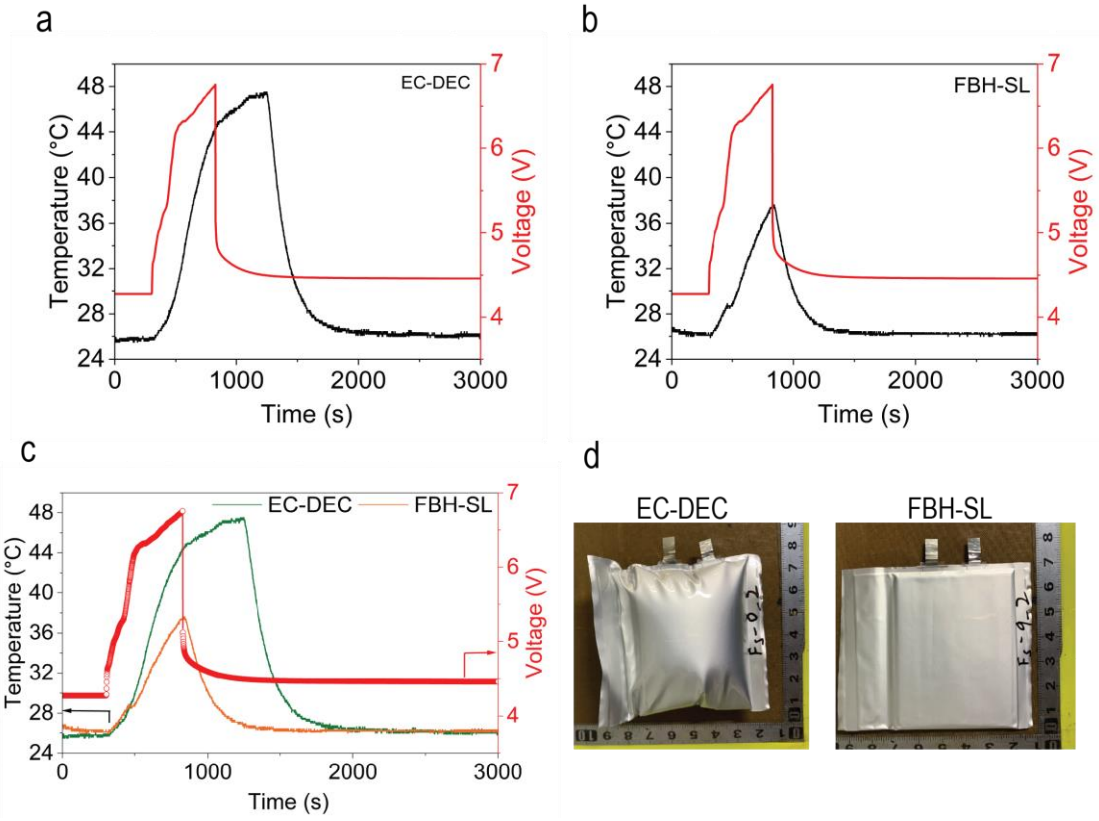

Fig. S47: Overcharge test of NCM811/Gr pouch cells with different electrolytes.

Video

Moive S1_Nail test_EC-DEC.mp4

SI Video 1: Nail test of NCM811/Gr pouch cell with EC-DEC electrolyte

Moive S2_Nail test_FBH.mp4

SI Video 2: Nail test of NCM811/Gr pouch cell with FBH electrolyte

Moive S3_Nail test_FBH-SL.mp4

SI Video 3: Nail test of NCM811/Gr pouch cell with FBH-SL electrolyte

Reference

1. A. Wang, L. Wang, Y. Wu, Y. He, D. Ren, Y. Song, B. Zhang, H. Xu and X. He, *Advanced Energy Materials*, 2023, **13**, 2300626.
2. M. Mao, X. Ji, Q. Wang, Z. Lin, M. Li, T. Liu, C. Wang, Y.-S. Hu, H. Li, X. Huang, L. Chen and L. Suo, *Nature Communications*, 2023, **14**, 1082.
3. O. Borodin, M. Olguin, P. Ganesh, P. R. C. Kent, J. L. Allen and W. A. Henderson, *Physical Chemistry Chemical Physics*, 2016, **18**, 164-175.
4. D. M. Seo, S. Reininger, M. Kutcher, K. Redmond, W. B. Euler and B. L. Lucht, *The Journal of Physical Chemistry C*, 2015, **119**, 14038-14046.
5. Y. Wu, A. Wang, Q. Hu, H. Liang, H. Xu, L. Wang and X. He, *ACS Central Science*, 2022, **8**, 1290-1298.
6. S. Pérez-Villar, P. Lanz, H. Schneider and P. Novák, *Electrochimica Acta*, 2013, **106**, 506-515.
7. C. C. Nguyen and B. L. Lucht, *Journal of The Electrochemical Society*, 2014, **161**, A1933-A1938.
8. D.-h. Yoon, M. Marinaro, P. Axmann and M. Wohlfahrt-Mehrens, *Journal of The Electrochemical Society*, 2018, **165**, A2467-A2469.
9. W. Lu, K. Xie, Z. x. Chen, Y. Pan and C. m. Zheng, *Journal of Fluorine Chemistry*, 2014, **161**, 110-119.

10. W. Lu, K. Xie, Y. Pan, Z.-x. Chen and C.-m. Zheng, *Journal of Fluorine Chemistry*, 2013, **156**, 136-143.
11. M. Morita, Y. Asai, N. Yoshimoto and M. Ishikawa, *Journal of the Chemical Society, Faraday Transactions*, 1998, **94**, 3451-3456.
12. Z. Chen, S. Liu, J. Huang, W. Huang, L. Chen, Y. Cui, Y. Du and R. Fu, *ACS Applied Materials & Interfaces*, 2021, **13**, 12025-12032.
13. T. T. Hagos, B. Thirumalraj, C.-J. Huang, L. H. Abrha, T. M. Hagos, G. B. Berhe, H. K. Bezabh, J. Cherng, S.-F. Chiu, W.-N. Su and B.-J. Hwang, *ACS Applied Materials & Interfaces*, 2019, **11**, 9955-9963.
14. S.-D. Han, J. L. Allen, E. Jónsson, P. Johansson, D. W. McOwen, P. D. Boyle and W. A. Henderson, *The Journal of Physical Chemistry C*, 2013, **117**, 5521-5531.
15. J. Chen, H. Zhang, M. Wang, J. Liu, C. Li and P. Zhang, *Journal of Power Sources*, 2016, **303**, 41-48.
16. Z. Wu, R. Li, S. Zhang, L. lv, T. Deng, H. Zhang, R. Zhang, J. Liu, S. Ding, L. Fan, L. Chen and X. Fan, *Chem*, 2023, **9**, 650-664.
17. C. Zhu, C. Sun, R. Li, S. Weng, L. Fan, X. Wang, L. Chen, M. Noked and X. Fan, *ACS Energy Letters*, 2022, **7**, 1338-1347.
18. W. Zhao, B. Zheng, H. Liu, F. Ren, J. Zhu, G. Zheng, S. Chen, R. Liu, X. Yang and Y. Yang, *Nano Energy*, 2019, **63**.
19. V. R. Rikka, S. R. Sahu, A. Chatterjee, P. V. Satyam, R. Prakash, M. S. R. Rao, R. Gopalan and G. Sundararajan, *The Journal of Physical Chemistry C*, 2018, **122**, 28717-28726.
20. Q. Wang, Z. Yao, C. Zhao, T. Verhallen, D. P. Tabor, M. Liu, F. Ooms, F. Kang, A. Aspuru-Guzik, Y.-S. Hu, M. Wagemaker and B. Li, *Nature Communications*, 2020, **11**, 4188.
21. Q. Li, Y. Wang, X. Wang, X. Sun, J. N. Zhang, X. Yu and H. Li, *ACS Appl Mater Interfaces*, 2020, **12**, 2319-2326.
22. B. Deng, H. Wang, W. Ge, X. Li, X. Yan, T. Chen, M. Qu and G. Peng, *Electrochimica Acta*, 2017, **236**, 61-71.
23. J. Fondard, E. Irisarri, C. Courrèges, M. R. Palacin, A. Ponrouch and R. Dedryvère, *Journal of The Electrochemical Society*, 2020, **167**.
24. B. Philippe, R. Dedryvère, M. Gorgoi, H. Rensmo, D. Gonbeau and K. Edström, *Chemistry of Materials*, 2013, **25**, 394-404.
25. W. Lu, S. Xiong, W. Pu, K. Xie and C. Zheng, *ChemElectroChem*, 2017, **4**, 2012-2018.